ROYAL SOCIETY
OF CHEMISTRY

PAPER

Check for updates

Electrochemical, surface, DFT, and ADMET insights into (*E*)-2-(2-hydroxybenzylidene)hydrazine-1-carboxamide as a corrosion inhibitor

Hind Boughazi, [ID] *ab Yamina Boudinar, [ID] ab Samira Tlili, [ID] c Amel Djedouani d and Noura Naili [ID] ae

In this work, (*E*)-2-((2-hydroxybenzylidene))hydrazine-1-carboxamide (HBHC) was investigated as a new organic and eco-friendly corrosion inhibitor for mild steel in acidic medium through electrochemical measurements including potentiodynamic polarization (PP), electrochemical impedance spectroscopy (EIS), long-term immersion tests, surface characterization, theoretical calculations, and ADMET studies. HBHC demonstrated excellent inhibition performance, achieving 94.50% efficiency by PP and 93.33% by EIS at 200 ppm, and retained remarkable stability over 30 days of immersion with 97.64% efficiency. Adsorption behavior was consistent with the Langmuir isotherm, with negative ΔG°_{ads} values indicating a mixed physisorption–chemisorption mechanism. SEM micrographs, EDX analysis, and elemental mapping analysis confirmed the formation of a uniform protective film enriched with heteroatoms on the steel surface. DFT calculations, including analysis of HOMO–LUMO frontier orbitals, revealed a low HOMO–LUMO energy gap (ΔE), supporting the high reactivity of HBHC and its strong donor–acceptor interactions with the Fe(110) surface, while MD simulations further confirmed its adsorption stability. Furthermore, ADMET predictions indicated low toxicity and good bioavailability, supporting the environmentally benign character of HBHC.

1. Introduction

Corrosion is a complex electrochemical process that causes metals and alloys to deteriorate through their interaction with aggressive environments.[1,2] Mild steel (MS), with a carbon content below 0.25%, is one of these metals that is often used because of its many beneficial characteristics, such as its affordability, excellent ductility, and high strength.[3] Its machinability and durability make it an ideal material for applications such as pipes, plates and beams for reinforcement in industries like construction, automobile production, and petrochemicals.[4] Mild steel, on the other hand, is highly susceptible to corrosion, particularly when it is exposed to acidic conditions such as the hydrochloric acid that is used in the cleaning, pickling and descaling operations.[4–6] Different techniques are used to mitigate corrosion, such as

electrochemical protection,[7,8] coatings,[9,10] and corrosion inhibitors. Of these methods, using corrosion inhibitors is very beneficial because it is affordable, effective, and practical.[11,12] a corrosion inhibitor is a specific chemical compound or a mixture of substances that, when present in the appropriate concentration and form in a given environment, prevents or reduces corrosion,[13,14] without causing a significant change in the concentration of corrosive agents.[15] Recent studies indicate a growing interest in using these inhibitors as a potential solution, due to their effectiveness over a broad temperature range, compatibility with protected materials, high water solubility, affordable cost, and relatively low toxicity.[16,17] They are able to adsorb on the surface, leading to the formation of a protective barrier that displaces water and safeguards the surface against deterioration. Effective organic inhibitors for corrosion incorporate elements such as nitrogen, oxygen, sulfur, and phosphorus.[18,19] Furthermore, these inhibitors can also contain structural moieties that have π-electrons, which work in conjunction with metal to facilitate the adsorption process.[18–20]

Hydrazine derivatives such as hydrazides, hydrazones, and hydrazinones are widely recognized as effective organic inhibitors for steel in acidic media.[21,22] Their efficiency is mainly attributed to electron-donating heteroatoms and conjugated systems that facilitate adsorption and the formation of stable protective layers. Literature reports indicate that these

aDepartment of Chemistry, Faculty of Sciences, University of 20 August 1955, Skikda 21000, Algeria. E-mail: h.boughazi@univ-skikda.dz; hind.boughazi21@gmail.com

bLaboratory of Physico-Chemistry Research on Surfaces and Interfaces, University of Skikda, 21000, ALgeria

cResearch Center in Industrial Technologies CRTI, Echahid Mohammed Abassi, BP. Box 64, Cheraga, 16014, Algiers, Algeria

dNormal Higher School Assia Djebar Constantine 3, 25000, Algeria

eResearch Unit of Environmental and Structural Molecular Chemistry, University of Constantine 1, Constantine 25000, Algeria

compounds generally act as mixed-type inhibitors, with inhibition mechanisms governed by physicochemical adsorption described by Langmuir or Temkin isotherms.[23–27] Their inhibition efficiencies are often high, with several studies reporting values above 95% at low concentrations.[28,29] The adsorption of these inhibitors generally depends on the molecular structure and the presence of functional groups such as methoxy, nitro, or thioamide moieties.[23,24,27,30,31] Quantum chemical calculations and molecular dynamics simulations have provided insight into the electronic properties and adsorption mechanisms, confirming that electron-donating groups and planarity enhance inhibitor performance.[27,29,30,32] Surface analyses (SEM, AFM) further confirm the formation of uniform, protective layers that mitigate corrosion damage.[19,21,26,29]

Cherrak *et al.* reported that 1,5-dimethyl-1*H*-pyrazole-3-carbohydrazide (PyHz) exhibited up to 96% inhibition efficiency in 1 M HCl, with Langmuir-type adsorption confirmed by electrochemical techniques, SEM/EDX, and theoretical approaches (DFT and Monte Carlo).[33] More recently, Kumari *et al.* investigated *N*′-[(4-methyl-1*H*-imidazole-5-yl)methylidene]-2-(naphthalen-2-yloxy)acetohydrazide (IMNH), which also displayed high anticorrosion activity in 1 M HCl, with efficiency increasing proportionally to concentration. EIS and PDP analyses confirmed its behavior as a Langmuir-type mixed inhibitor, while SEM and AFM observations revealed a smoother and less damaged surface for the inhibited steel.[34] Collectively, these studies underline the strong potential of hydrazone and hydrazide derivatives as promising corrosion inhibitors in acidic environments. In general, hydrazide derivatives have emerged as highly efficient organic corrosion inhibitors. Their protective action is attributed to adsorption involving electrostatic interactions, coordination bonds, and the presence of aromatic or polar functional groups, leading to dense protective films. These features make them attractive alternatives to conventional inhibitors for safeguarding metallic infrastructures in aggressive acidic environments.

In this context, the present study investigates the efficiency of a novel organic inhibitor, HBHC [(*E*)-2-(2-hydroxybenzylidene) hydrazine-1-carboxamide], for the protection of A179 mild steel in an acidic medium. HBHC was selected as a corrosion inhibitor because of its multifunctional structure, which offers several adsorption centers. The hydrazine core (–NH–NH–) contains nitrogen atoms with lone pairs of electrons that serve as active sites for coordination with vacant d-orbitals of the metal surface. The aromatic benzylidene ring enhances π–electron interactions, while the hydroxyl substituent increases polarity and facilitates hydrogen bonding and additional coordination. Finally, the carboxamide group (–CONH$_2$) contributes to molecular stability and promotes the cohesion of the protective film. These synergistic features make HBHC a strong candidate for efficient corrosion inhibition. Previous studies have reported that hydrazide derivatives, structurally related to HBHC, act as efficient corrosion inhibitors in acidic environments. However, many of these compounds still suffer from limitations such as toxicity, environmental concerns, moderate efficiency, or poor long-term stability. To the best of our knowledge, the corrosion inhibitive performance of HBHC

on mild steel in acidic medium has not yet been explored. This study addresses that gap by demonstrating that HBHC combines strong adsorption capacity with long-term stability while maintaining an environmentally benign and non-toxic profile. Moreover, through the integration of electrochemical measurements, surface characterization, theoretical simulations, and ADMET studies as a new dimension in corrosion inhibitor research, the work delivers comprehensive mechanistic and safety insights that distinctly differentiate HBHC from previously reported hydrazide-based inhibitors.

2. Experimental

2.1. Characterization of the inhibitor

The tested inhibitor is a new compound named (*E*)-2-(2-hydroxybenzylidene)hydrazine-1-carboxamide (HBHC). The structure is depicted in Fig. 1. The compound is a whitish powder with a molar mass of 179.07 g mol^{-1}. The structure of this compound was confirmed through FTIR analysis, illustrated in Fig. 2.

2.2. Mild steel samples preparation

The material chosen for this study is A179 mild steel, with its chemical composition (in weight percent) provided in Table 1. The metal was cut using a machine that employs a cooling fluid
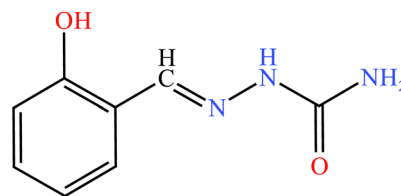

Fig. 1 Molecular structure of (*E*)-2-(2-hydroxybenzylidene)hydrazine-1-carboxamide HBHC; formula = C$_8$H$_9$N$_3$O$_2$, molar mass = 179.07 g mol^{-1}.
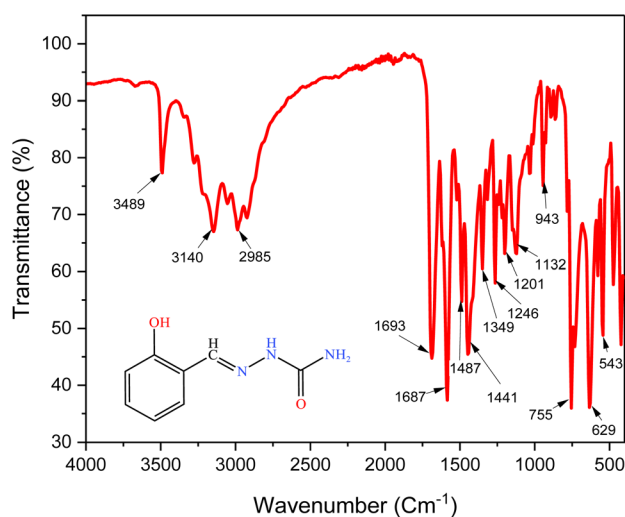

Fig. 2 FTIR spectrum for HBHC substance.

Table 1 Elemental composition of A179 carbon steel

Element	C	Mn	Si	S	P	Fe
Value (%)	0.06–0.18	0.27–0.63	0.25 max	0.035 max	0.035 max	Rest

to reduce mechanical damage. It was then attached to a copper wire and encased in resin, leaving a 1 cm^2 surface of the metal exposed to the acidic environment.

The surface was prepared by polishing with SiC papers (400–2000 grit), then washed with distilled water, rinsed with acetone, rinsed again with distilled water, and finally dried under an air stream.

2.3. Test solution

The corrosion inhibition study was conducted using a 1 M HCl solution (pH approximately 1) as the corrosive medium. This solution was prepared by diluting reagent-grade hydrochloric acid (37 wt%) with distilled water. The experiments were performed at a controlled temperature of 298 K (approximately 25 °C) to closely reflect standard room conditions, enabling the simulation of corrosion behavior under conditions representative of a wide range of practical applications and environmental exposures. HBHC solutions at different concentrations (ranging from 50 to 200 ppm) were prepared by dissolving the inhibitor in 1 M HCl, with 10% dimethyl sulfoxide (DMSO) used as an organic solvent to enhance solubility.

2.4. Electrochemical measurements

The electrochemical investigations were carried out within a conventional three-electrode configuration, employing a platinum counter electrode and an Ag/AgCl reference electrode in a saturated KCl solution, and the working electrode is a square-shaped steel surface (1 × 1 cm^2) coated with resin.

The polarization experiments and electrochemical impedance spectroscopic investigations (EIS) were performed using an AUTOLAB model PGSTAT 302 N. Data were analyzed using Nova 2.1.4 software.

The electrochemical measurement and polarization corrosion experiments were conducted in a 1 M HCl solution, with two essential parameters being modified:

• The influence of the HBHC inhibitor concentration was examined by immersing the electrode in solutions with concentrations ranging from 0 to 200 ppm at room temperature.

• The influence of immersion duration on the corrosion inhibition performance of HBHC at optimal concentration (200 ppm).

Initially, a steady-state open circuit potential (E_{ocp}) was established by immersing the working electrode in the test solutions for 30 minutes. Subsequently, potentiodynamic polarization curves were acquired at a scan rate of 0.5 mV s^{-1} within a potential range of ±250 mV relative to the E_{ocp}. Corrosion current density values were determined by extrapolating the anodic and the cathodic Tafel lines to their intersection at the corrosion potential (E_{corr}).

The inhibition efficiency (IE %) was calculated using eqn (1) based on data obtained from the Tafel plots:[35]

$$IE(\%) = \left(1 - \left(\frac{i_{corr}^{inh}}{i_{corr}^{0}}\right)\right) \times 100 \qquad (1)$$

Here, i_{corr}^{0} and i_{corr}^{inh} represent the current density in bot uninhibited and inhibited solutions, respectively.

The EIS measurements were carried out in the range from 10^5 Hz to 10^{-1} Hz, with a 10 mV sinusoidal signal perturbation. The frequency points per decade were set at 10 points per decade. The resulting data were utilized to estimate the inhibition effectiveness (E_{EIS}) using the following expression:[35]

$$IE(\%) = \frac{R_{ct} - R_{ct}^{0}}{R_{ct}} \times 100 \qquad (2)$$

where R_{ct} and R_{ct}^{0} denote the charge transfer resistances in HCl solution with and without HBHC inhibitor, respectively.

2.5. Surface analysis

A179 carbon steel specimens were immersed in 1 M HCl solution for durations of 1 day and 30 days at room temperature, both in the absence and presence of the HBHC inhibitor at its optimal concentration (200 ppm). Prior to immersion, each specimen was individually prepared, thoroughly cleaned, and rinsed with distilled water before drying. The surface morphologies of the inhibited and uninhibited samples were analyzed using a Quanta FEG-250 scanning electron microscope (SEM) operated at an accelerating voltage of 20 kV. Additionally, the chemical composition and the surface mapping of the examined surface areas were determined using Energy Dispersive X-ray Spectroscopy (EDX).

2.6. Quantum chemical study

Computational calculations were conducted to complement and interpret the experimental findings. The main objective of these theoretical analyses was to elucidate the structural features of the organic corrosion inhibitors, clarify their inhibition mechanisms, and provide a molecular-level explanation of their coordination with the metal surface. This integrated approach offers valuable insights into how these molecules achieve optimal corrosion protection.

2.6.1. Theoretical approach and computational details. The adsorption mechanism of the HBHC molecule, in both its neutral and protonated forms, on the Fe(110) surface was investigated using density functional theory (DFT) at the M06-2X/6-31G(d) level, as implemented in Gaussian 09.[36,37] All calculations were carried out in the aqueous phase employing the conductor-like polarizable continuum model (CPCM) to accurately represent corrosion conditions.[38]

Key quantum chemical descriptors were calculated, including ionization potential (I), electron affinity (A), chemical hardness (η), electronegativity (χ), softness (σ), electrophilicity index (ω), and chemical potential (ε), computed using standard equations[39,40] (eqn (3)–(9)).

$$I = -E_{HOMO} \tag{3}$$

$$A = -E_{LUMO} \tag{4}$$

$$\eta = (I - A)/2 \tag{5}$$

$$\chi = (I + A)/2 \tag{6}$$

$$\sigma = 1/\eta \tag{7}$$

$$\omega = \chi^2/(2\eta) \tag{8}$$

$$\varepsilon = -\chi \tag{9}$$

where E_{HOMO} and E_{LUMO} are the energies of the highest occupied and lowest unoccupied molecular orbitals, respectively, and $\chi_{Fe(110)}$ and $\eta_{Fe(110)}$ are the electronegativity and hardness of the Fe(110) surface. The electron transfer fraction (ΔN_{110}) from the organic molecule (HBHC) to the Fe(110) metal surface was estimated using the electronegativity and hardness values of both species:[39]

$$\Delta N_{110} = (\chi_{Fe(110)} - \chi_{HBHC})/[2 \times (\eta_{Fe(110)} + \eta_{HBHC})] \tag{10}$$

Here, $\chi_{Fe(110)} = 4.82$ eV represents the electronegativity of the Fe(110) surface, derived from its work function, which theoretically explains the surface electronegativity.[41] This electron transfer represents the movement of charge from the filled orbitals of the organic molecule to the empty orbitals of the metal surface, highlighting the interaction strength and the charge redistribution that occurs at the interface. To better understand the specific reactive sites within inhibitory molecules, the analysis of Fukui indices is essential. These indices identify regions that are likely to undergo electrophilic, nucleophilic, or radical attack, depending on the change in electron density upon the gain or loss of an electron.[42,43]

The Fukui indices are defined as follows:[39]

For a nucleophilic attack (addition of an electron) on atom k:

$$f_k^+ = q_k(N + 1) - q_k(N) \tag{11}$$

• For an electrophilic attack (removal of an electron) on atom k:

$$f_k^- = q_k(N) - q_k(N - 1) \tag{12}$$

• For a radical attack (average variation) on atom k:

$$f_k^0 = [q_k(N + 1) - q_k(N - 1)]/2 \tag{13}$$

where $q_k(N)$, $q_k(N + 1)$, and $q_k(N - 1)$ represent the atomic charges on atom k in the neutral, anionic, and cationic states, respectively. These indices make it possible to determine the

sites most likely to interact with the metal surface, and thus the preferential localization of inhibition. Additionally, the molecular electrostatic potential (ESP) is another property calculated *via* Density Functional Theory (DFT), representing the distribution of the electric potential generated by the molecule in its surroundings. The calculation of ESP enables the identification of regions with high electron density (nucleophilic zones) and electron-deficient regions (electrophilic zones).[41,44] The ESP at a point r in space is defined by the eqn (14):[44]

$$V(r) = \Sigma Z_a/|R_a - r| - \int[\rho(r')/|r' - r|]dr' \tag{14}$$

where: Z_a is the nuclear charge of atom A located at R_a; $\rho(r')$ is the electron density at position r'.

The first sum represents the positive contribution of the nuclei. The integral represents the negative contribution of the electrons. Analysis of the ESP map allows for the visual identification of active sites for inhibitor metal surface interaction, as these sites are generally correlated with regions of high negative potential, favoring coordination to metal atoms.[43]

2.6.2. Monte Carlo (MC) simulations. The Monte Carlo method was employed to simulate the statistical adsorption of inhibitors on steel surfaces, evaluating the configuration and thermodynamic stability of the resulting molecular complexes. This stochastic technique helps to elucidate the spatial distribution and surface coverage density of inhibitors, which are key factors in determining the effectiveness of anticorrosion protection.[45]

2.6.3. Molecular dynamics (MD). Molecular dynamics (MD) is a powerful computational method for studying how molecules behave on metal surfaces under different thermodynamic conditions, such as changes in temperature and pressure. This technique provides clear insights into the stability and movement of inhibitor molecules, as well as the durability of the protective layers they form against external disturbances.[46,47]

In this research, the interactions between the studied molecules and the Fe(110) surface were examined using molecular dynamics (MD) simulations with the Forcite module in Materials Studio 2023. The simulation cell measured $24.82 \times 24.82 \times 30$ Å^3 and included 621 water molecules, 9 chloride ions (Cl$^-$), and 9 hydronium ions (H$_3$O$^+$). The simulation ran for 500 picoseconds (ps) with a time step of 1.0 femtosecond (fs), while the temperature was maintained at 300 K using the *NVT* ensemble and the Andersen thermostat. The COMPASS III force field was applied to accurately model the interactions within the system. This approach allows for a detailed and reliable analysis of molecular behavior at the metal–solution interface, supporting a better understanding of corrosion inhibition mechanisms.[43]

3. Results and discussion

3.1. FTIR spectra of HBHC

The FTIR analysis illustrated in Fig. 2 highlights significant absorption peaks associated with essential functional groups, thereby substantiating the molecular identity of the compound. A band at 3489 cm^{-1} is attributed to O–H stretching vibrations,

indicating the presence of a phenolic hydroxyl group. The peak at 3140 cm^{-1} corresponds to N–H stretching, consistent with the hydrazide moiety in the structure. The absorption at 2985 cm^{-1} is associated with C–H stretching in aliphatic or aromatic systems. A strong band at 1693 cm^{-1} is assigned to C=O stretching, confirming the presence of a carbonyl group, while the adjacent peak at 1687 cm^{-1} is attributed to C=N stretching. The peaks observed at 1487 cm^{-1} and 1441 cm^{-1} are due to aromatic C=C stretching vibrations.

Absorptions in the range of 1349–1132 cm^{-1} are indicative of C–N, N–N, and C–O stretching modes, reflecting the presence of amine and phenolic functionalities. Finally, the bands at 943, 755, 629, and 543 cm^{-1} correspond to aromatic C–H out-of-plane bending vibrations, confirming the aromatic nature of the compound. Collectively, the FTIR data support the proposed molecular structure and confirm the presence of hydroxyl, carbonyl, imine, amine, and aromatic functional groups.

3.2. Effect of inhibitor concentration

3.2.1. OCP measurement.
Open circuit potential (OCP) measurements are widely used in electrochemical studies to assess the corrosion behavior of metallic materials in various environments. By monitoring the potential of a metal surface over time in the absence of an external current, OCP curves were recorded to evaluate the effect of different concentrations of a corrosion inhibitor on the electrochemical stability of the metal surface. Fig. 3 illustrates the OCP curves of A179 in an HCl medium under various concentrations at 298 K, both in the absence and presence of the HBHC inhibitor. The open circuit potential (OCP) graph shows the evolution of potential over time for samples containing increasing concentrations of HBHC inhibitor (from 0 to 200 ppm). A progressive shift toward more positive potentials is observed with increasing inhibitor concentration, indicating the adsorption of protective inhibitor molecules and suggesting enhanced corrosion resistance of the metal surface. Notably, the sample with 200 ppm exhibits the
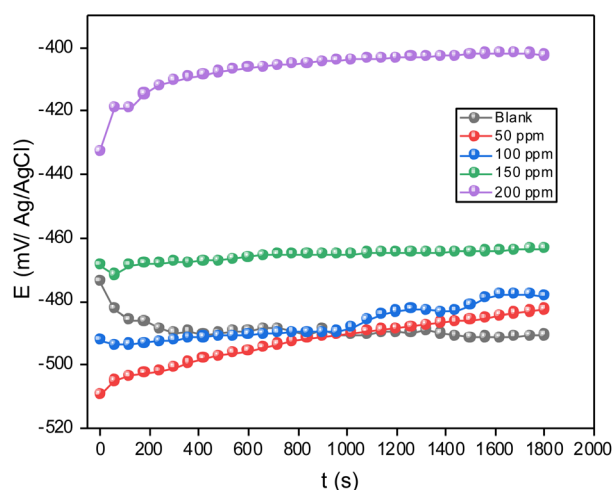
most noble potential (around −401 mV *vs.* Ag/AgCl), which indicates the formation of an effective protective film on the metal surface. In contrast, the blank sample (without inhibitor) shows a more negative potential (around −490 mV), which reflects active corrosion. Additionally, the stabilization of the potential over time indicates that the system reaches electrochemical equilibrium.[44]

Overall, the OCP curves highlight the increasing effectiveness of the inhibitor, with optimal performance observed at 200 ppm.

3.2.2. Potentiodynamic polarization measurements.
Tafel polarization measurements are a key electrochemical technique used to evaluate metal corrosion characteristics and the efficiency of corrosion inhibitors. They involve applying a controlled potential sweep and measuring the resulting current. In Fig. 4, Tafel polarization curves were recorded for an A179 carbon steel substrate in a 1 M HCl solution for various concentrations of HBHC inhibitor at ambient temperature. Table 2 summarizes corresponding electrochemical parameters, including corrosion potential (E_{corr}), corrosion current density (i_{corr}), anodic and cathodic Tafel slopes (β_a and β_c), and inhibition efficiency (IE %).

An initial analysis of these curves shows that the addition of the inhibitor affects both the anodic and cathodic reactions.

In the 1 M HCl solution, the inhibitor reduces the anodic partial current associated with metal dissolution and the reduction in the cathodic current corresponds to a decrease in proton concentration.

The cathodic curves present a linear Tafel region, confirming that the hydrogen evolution reaction on the steel is controlled entirely by activation.[48,49] The Tafel polarization curves show the influence of different concentrations of the corrosion inhibitor on the electrochemical behavior of the metal surface. As the inhibitor concentration increases, a noticeable decrease in the
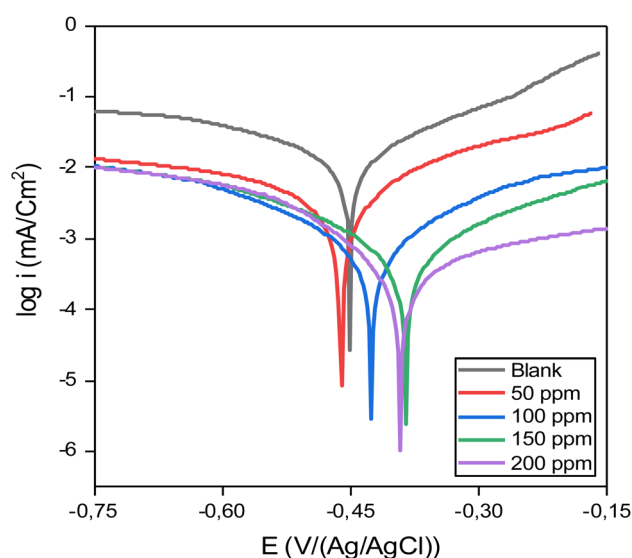

Fig. 3 Open circuit potential curves of A179 carbon steel potential without and with different concentrations of HBHC inhibitor at 25 °C.

Fig. 4 Potentiodynamic polarization curves of A179 in a 1 M HCl solution in the absence and presence of HBHC at different concentrations at 298 K.

Table 2 Polarization parameters of A179 carbon steel corrosion in 1 M HCl with varying concentrations of HBHC

Medium	E_{corr} (mV/Ag/AgCl)	i_{corr} (μA cm^{-2})	β_c (mV dec^{-1})	β_a (mV dec^{-1})	R_p (Ω)	Surface coverage (θ)	IE (%)
Blank	-451.01 ± 10.42	7.001 ± 0.08	338.6	200.64	8420 ± 78	—	—
50 ppm	-460.53 ± 8.47	3.567 ± 0.11	344.2	183.48	$15\,093 \pm 44$	0.4905	49.05
100 ppm	-425.53 ± 12.44	2.0516 ± 0.07	332.96	175.25	$38\,336 \pm 125$	0.7069	70.69
150 ppm	-385.28 ± 7.85	1.2644 ± 0.04	356.34	156.34	$45\,112 \pm 182$	0.8194	81.94
200 ppm	-390.93 ± 8.77	0.3848 ± 0.02	302.51	81.22	$51\,679 \pm 104$	0.9450	**94.50**

corrosion current density (i_{corr}) is observed, showing a notable decrease in the rate of corrosion. Among the tested concentrations, 200 ppm is the optimal inhibitor concentration, demonstrating the lowest (i_{corr}) value and a notable shift in the corrosion potential (E_{corr}) toward more noble values, indicating enhanced protection of the surface. The calculated inhibition efficiency at this concentration is 94.50%, providing excellent corrosion inhibition under the studied conditions.

Table 2 demonstrates that even a small amount of the inhibitor significantly reduces the corrosion current density (i_{corr}). The i_{corr} of the blank solution decreases from 7.001 μA cm^{-2} to 0.3848 μA cm^{-2} with the addition of 200 ppm of HBHC. Furthermore, polarization resistance (R_p) increases considerably, rising from 8420 Ω cm^2 to 51 679 Ω cm^2 without and with the inhibitor at 200 ppm, respectively. Table 2 also indicates that HBHC acts as a mixed-type inhibitor. This is evidenced by the fact that the variation in corrosion potential (E_{corr}) in the presence of the inhibitor is less than 85 mV compared to the blank value.[31,50,51] In the present case, the maximum displacement is less than 70 mV vs. Ag/AgCl. Additionally, both anodic and cathodic partial current densities are significantly decreased, indicating that the inhibitor effectively suppresses both anodic metal dissolution and cathodic reduction reactions.

The reduction in the corrosion rate due to the adsorption of inhibitors on the metal surface is a clear indicator that the inhibitor molecules are successfully protecting the metal. The type of adsorption, whether physisorption, chemisorption, or a combination of both, determines the strength, reversibility, and longevity of the corrosion protection.[52] The functional groups in HBHC inhibitor, such as oxygen and nitrogen, facilitate the adsorption of the inhibitor molecules onto the mild steel surface.[53] The interactions formed between the inhibitor and the metal surface lead to a robust and stable protective layer that decreases the corrosion rate, positioning HBHC as an efficient corrosion inhibitor. This protective mechanism guarantees extended corrosion protection by preventing corrosive agents from reaching the metal surface.

3.2.3. Electrochemical impedance spectroscopy (EIS). Electrochemical impedance spectroscopy (EIS) is a widely recognized and powerful technique for investigating corrosion mechanisms, offering valuable information on surface characteristics. Fig. 5a and b presents Nyquist and Bode plots of carbon steel A179 in a 1 M HCl solution both before and after the addition of varying concentrations of HBHC inhibitor.

The impedance spectra in the absence of HBHC present one capacitive loop, which depicts a depressed semicircle adjusted with electrical circuit Fig. 6a. The depressed semicircle is attributed to the frequency dispersion effect and surface irregularities and heterogeneities.[29,54] This loop can be attributed to a charge transfer process.

In the presence of the HBHC inhibitor, examination of the impedance spectra reveals the presence of two distinct loops. The first loop, observed at high frequencies, is associated with
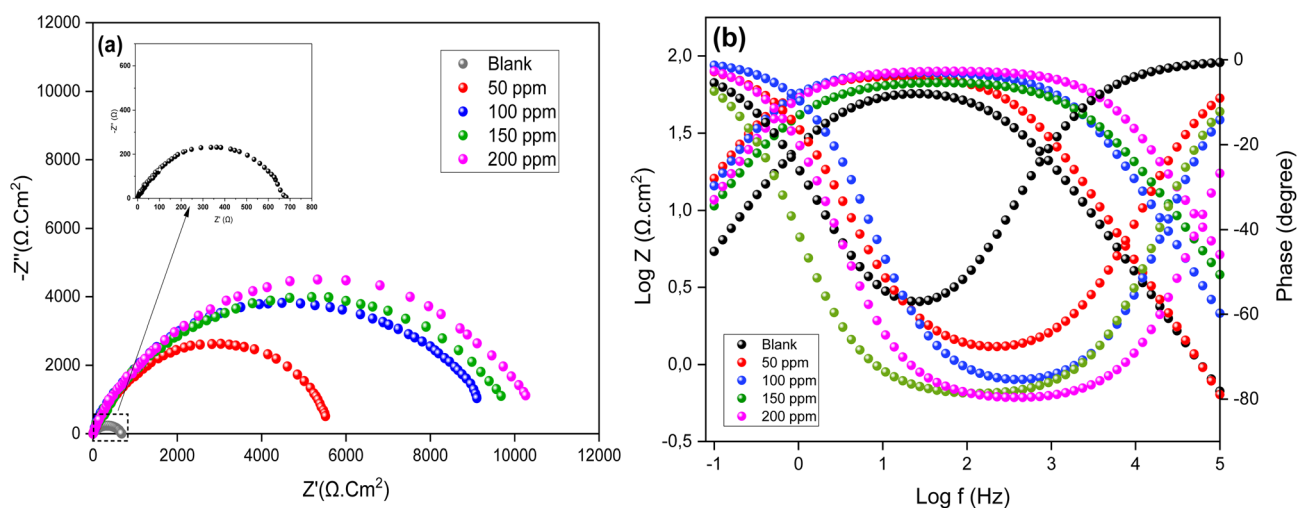

Fig. 5 Nyquist diagrams (a) and Bode diagrams (b) of A179 carbon steel in 1 M HCl solution in the absence and presence of HBHC at different concentrations after 1 h of immersion at 25 °C.
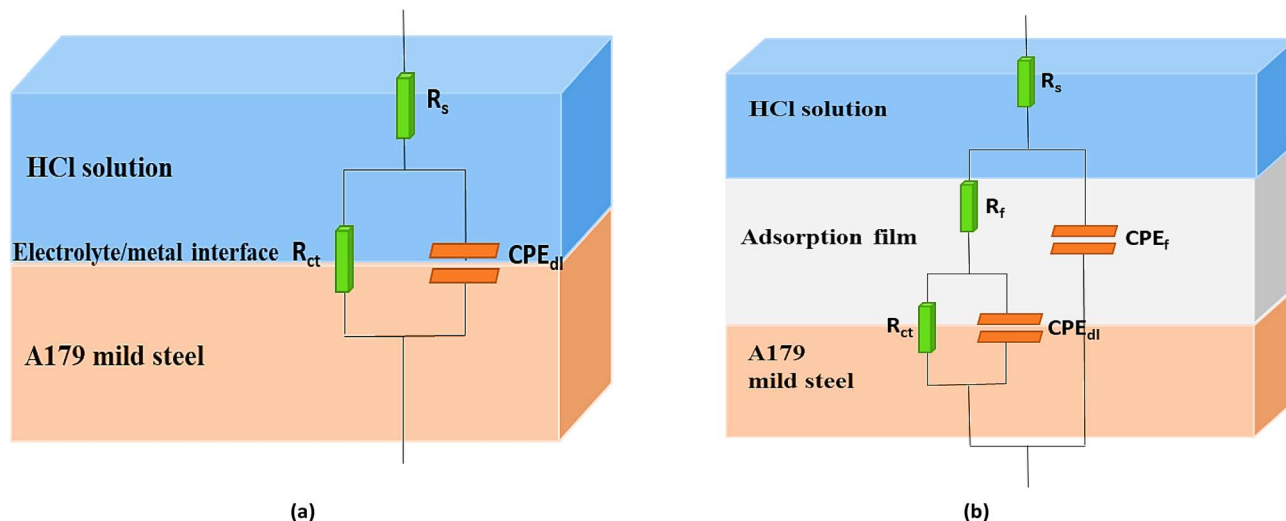
Fig. 6 Equivalent circuit used to fit EIS data (a) without and (b) with HBHC inhibitor.

the adsorption of the inhibitor film, whereas the second loop, at low frequencies, corresponds to the charge-transfer processes occurring at the metal/electrolyte interface. An increase in the size of the loops is noted as the inhibitor concentration increases. This result suggests that the inhibitor completely changes the corrosion process at the A179 carbon steel/1 M HCl solution interface.

Fig. 5b presents the Bode plots for A179 steel in the absence and presence of various concentrations of HBHC. An increase in log(Z) values, accompanied by a shift toward lower frequency values, is observed with rising inhibitor concentrations. This phenomenon can be associated with the development of a protective film on the A179 steel surface.[55] On the other hand, the phase angle values increase up to a more negative value of $-80°$ for an optimal concentration of 200 ppm compared to the blank (around $-50°$), which implies that the tested inhibitor is effective.[49]

Fig. 6a presents the equivalent circuit (EC) employed to analyze the impedance spectra in the absence of the inhibitor. In this model, the constant phase element (CPE) is introduced in place of the ideal double-layer capacitance, owing to the depressed capacitive semicircles observed in the Nyquist plots. The use of CPE in such circuits is a well-established practice in corrosion studies, as the measured macroscopic impedance is strongly influenced by various microscopic factors, including surface roughness, charge inhomogeneities, and complex

electrochemical reactions. The circuit elements consist of the solution resistance (R_s), the constant phase element (CPE) and the charge-transfer resistance (R_{ct}).

The equivalent electrical circuit (shown in Fig. 6b) was proposed to fit the EIS data in presence of HCBC inhibitor, the high-frequency loop is modeled by a Constant Phase Element of the film (CPE$_f$), which accounts for the non-ideal capacitive behavior of the protective layer, connected in parallel with the film resistance (R_f). The double-layer Constant Phase Element (CPE$_{dl}$) in parallel with the charge-transfer resistance (R_{ct}) represents the low-frequency loop.

From the electrochemical parameters obtained by fitting the experimental data with the equivalent circuit (Table 3), it can be observed that the capacitance of the constant phase element of the double layer (CPE$_{dl}$) decreases with increasing inhibitor concentration, while the charge transfer resistance (R_{ct}) increases. This behavior is attributed to the gradual replacement of water molecules by HBHC inhibitor molecules at the electrode surface, which reduces the number of active sites and thereby retards the corrosion process.[56] Finally, the inhibition efficiency (IE %) for metal corrosion, calculated using eqn (2), in the presence of HBHC increases with rising inhibitor concentration. This indicates that a greater number of inhibitor molecules are able to adsorb onto the metal surface, thereby forming a thicker surface film or enhancing surface coverage.[57] The value of the inhibition efficiency reached a maximum of

Table 3 EIS parameters of corrosion inhibition of A179 carbon steel with and without HBHC inhibitor in a 1 M HCl at different concentrations

| C (ppm) | R_s (Ω cm^2) | CPE$_f$ | | | R_f (Ω cm^2) | CPE$_{dl}$ | | R_{ct} (Ω cm^2) | IE (%) |
		Q_f (F s^{n-1}) $\times 10^{-7}$	n			Q_{dl} (F s^{n-1}) $\times 10^{-4}$	n		
Blank	2.78 ± 0.07	—	—	—		2.291 ± 1.658	0.898 ± 0.012	666.1 ± 29.3	—
50 ppm	3.45 ± 1.05	2.87 ± 0.45	0.964 ± 0.005	$337,4 \pm 28.27$		0.838 ± 0.781	0.864 ± 0.023	5251.9 ± 55.3	87.32
100 ppm	2.47 ± 0.14	0.755 ± 0.385	0.974 ± 0.025	477.8 ± 71.8		0.571 ± 0.568	0.875 ± 0.011	8952.7 ± 75.2	92.55
150 ppm	3.54 ± 0.05	0.581 ± 0.104	0.988 ± 0.001	510.8 ± 124.9		0.327 ± 0.711	0.858 ± 0.014	9551.4 ± 122.4	93.03
200 ppm	3.61 ± 0.12	0.302 ± 0.021	0.989 ± 0.002	582.9 ± 135.2		0.192 ± 1.025	0.839 ± 0.035	9998.6 ± 107.9	93.33

93.33% of effectivity at 200 ppm. Furthermore, Table 3 shows that the electrolyte resistance R_s remains nearly constant across different HBHC concentrations, indicating that the inhibitor does not significantly affect the solution conductivity.[58,59]

The electrochemical performance of HBHC was compared with literature data for structurally related hydrazide derivatives. Abdallah *et al.* reported inhibition efficiencies of 92–93% for H$_2$HEH and H$_2$MEH in 1 M HCl, with R_{ct} values up to 7285 Ω cm^2 at 10^{-4} M. In our study, HBHC achieved similar efficiencies (93%) but with higher R_{ct} values (9998.6 Ω cm^2 at 200 ppm). This close agreement indicates that HBHC follows a comparable inhibition mechanism to other nitrogen-rich hydrazide derivatives, supporting the reliability of our findings.[60]

3.3. Adsorption isotherm analysis

Adsorption thermodynamics is commonly applied in relevant studies to describe the corrosion inhibitor adsorption behavior or the interaction between metal and inhibitor. The calculated thermodynamic parameters of adsorption play an essential part in comprehending the adsorption process of the metal surface. In many cases, it is for parameters such as the adsorption equilibrium constant (K_{ads}) and adsorption free energy (ΔG°_{ads}) that the adsorption types of an inhibitor on the metal surface (*i.e.*, physisorption or chemisorption, or both) can be distinguished.[61] The objective of this study is to know more details on the mechanism of adsorption of HBHC inhibitor on the surface of A179 carbon steel. The analysis of adsorption isotherms provides insight into how the organic molecule adsorbs onto the metal surface to reduce corrosion.[62] Using the inhibitor concentrations and surface coverage θ presented in Table 3, the experimental data were fitted to different adsorption models, such as Langmuir, Freundlich, Temkin, and Frumkin, and the best correlation was found with Langmuir's adsorption isotherm, as illustrated in Fig. 7.

Mathematically, Langmuir's adsorption isotherm is expressed as in eqn (15):[63]

$$\frac{C_{inh}}{\theta} = \frac{1}{K_{ads}} + C_{inh} \tag{15}$$

where K_{ads} represents the Langmuir adsorption constant, C_{inh} is the inhibitor concentration in the corrosive medium, and θ denotes the fraction of the surface covered by the inhibitor.

On the other hand, the Freundlich isotherm describes multilayer adsorption of the tested inhibitor onto the steel surface, and it can be expressed in linear form by eqn (16) as follows:[64]

$$\log\theta = \log K_f + \frac{1}{n}(\log C_{inh}) \tag{16}$$

where K_f represents the Freundlich equilibrium constant, C is the inhibitor concentration, θ is the surface coverage, and $1/n$ reflects surface heterogeneity.

The Temkin isotherm considers the enthalpy change due to inhibitor interactions. Where all molecules in the layer decrease linearly with coverage due to inhibitor–inhibitor interactions, and can be explained in linear form by eqn (17) as follows:[64]

$$\theta = \frac{RT}{b}\ln(k) + \frac{RT}{b}\ln(C_{inh}) \tag{17}$$

where θ is the surface coverage, b is the adsorption potential, R is the gas constant, T is the temperature, and K is the equilibrium constant.

The Frumkin isotherm includes an interaction parameter to account for attractions or repulsions between adsorbed inhibitor molecules. This can be expressed in linear form by eqn (18) as follows:[64]

$$\ln\left(\frac{\theta}{1-\theta}\right) = \ln(K_{ads}) + 2a\theta \tag{18}$$

where C_{inh} is the inhibitor concentration, θ is the surface coverage, K_{ads} is the equilibrium constant, and a is the interaction parameter.

In Fig. 7, the Langmuir plot consists of a straight line with a 0.9999 regression coefficient. The slope values that were obtained were close to 1, which validated the plot's well-fitting value.[64] The ratio $1/K_{ads}$ corresponds to the intercept of the Langmuir isotherm (Fig. 7a). The adsorption equilibrium constant K_{ads} obtained from this intercept was subsequently used to calculate the standard free energy of adsorption ΔG°_{ads} using eqn (19).[65]

$$\Delta G^{\circ}_{ads} = -RT\ln(55.5K_{ads}) \tag{19}$$

where R is the universal gas constant (8.314 J mol^{-1} K^{-1}), T is the absolute temperature, and 55.5 mol L^{-1} is the concentration of water at 298 K.

According to the Langmuir isotherm, adsorption occurs as a monolayer of inhibitor molecules uniformly covering distinct adsorption sites on the metal surface, where each adsorption site holds only one inhibitor molecule, with no interaction between adsorbed molecules.[66,67]

The value of K_{ads} is 44 752.74 L mol^{-1}. The high value of adsorption equilibrium constant K_{ads} shows good adsorption of the HBHC inhibitor.[68] The nature of the adsorption process was further evaluated through thermodynamic analysis; the standard Gibbs free energy of adsorption ΔG°_{ads} provides insight into the spontaneity of the adsorption process and the nature of the adsorption mechanism. The resulting ΔG°_{ads} was found to be -36.483 kJ mol^{-1}. A negative ΔG°_{ads} value confirms the spontaneous adsorption of the HBHC inhibitor onto the steel surface and implies a strong interaction between the inhibitor molecules and the metal substrate.[69] Generally, ΔG°_{ads} values less than or equal to -20 kJ mol^{-1} are indicative of physisorption, which involves weak van der Waals forces, whereas values equal to or more negative than -40 kJ mol^{-1} are characteristic of chemisorption, where stronger chemical bonds are formed. In this study, the calculated ΔG°_{ads} of -36.483 kJ mol^{-1} indicates that the adsorption of HBHC is thought to involve two different types of interaction: chemisorption and physisorption, since this value is close to the chemisorption threshold, it can be concluded that adsorption is mainly dominated by chemisorption.[67,70] This is common for organic inhibitors that interact with metal surfaces through mechanisms like electron donation, π–π interaction, or coordination with metal sites.[71,72]
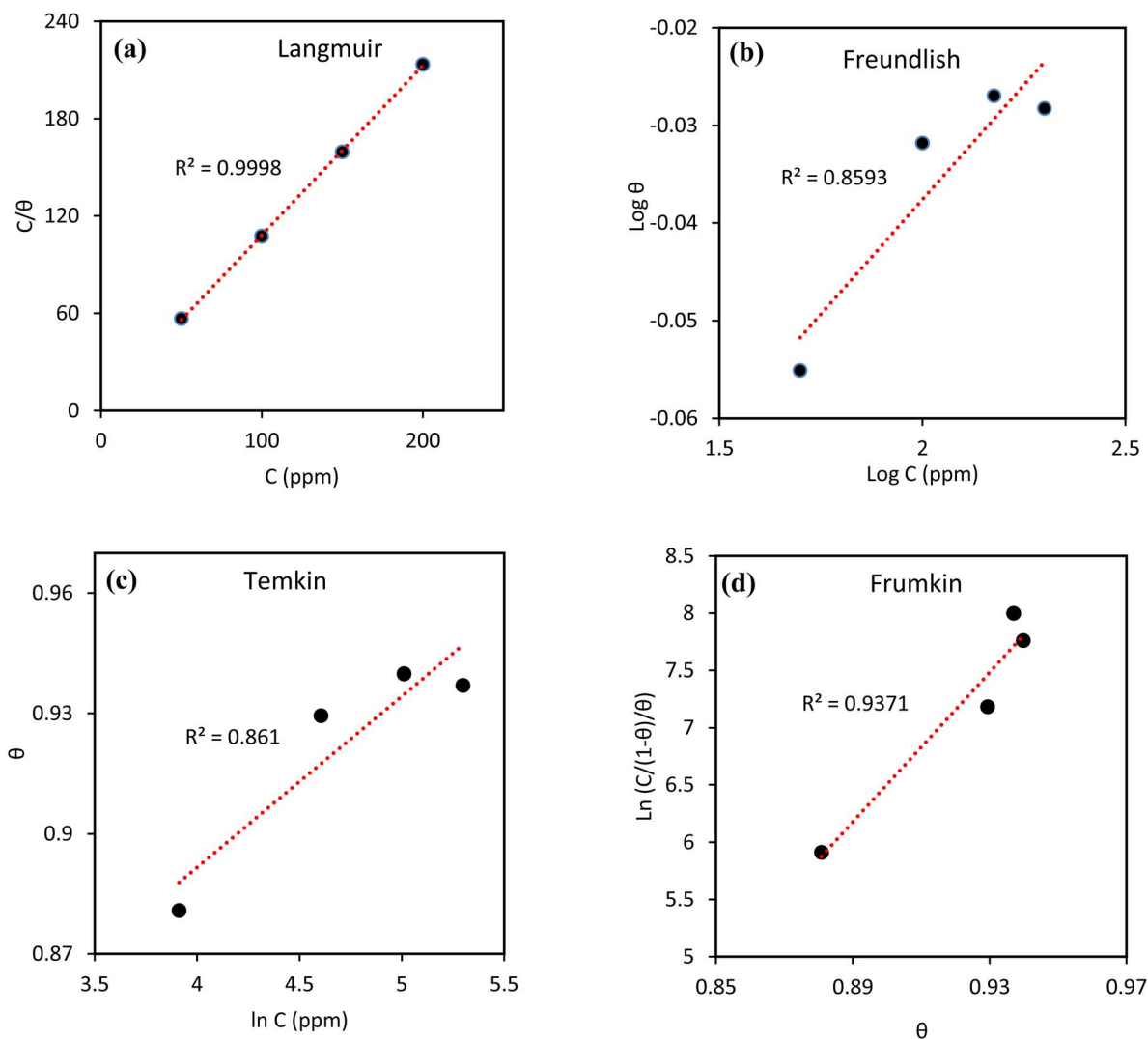
Fig. 7 Adsorption isotherms (a) Langmuir, (b) Freundlish, (c) Temkin, and (d) Frumkin for A179 MS in 1 M HCl inhibited by 200 ppm of HBHC at 298 K.

3.4. Impact of immersion duration

Fig. 8 shows electrochemical impedance diagrams obtained on A179 carbon steel in 1 M HCl in the presence of 200 ppm of HBHC immersed for 1, 6, 12, 18, 24, and 30 days at 298 K. This study aimed to evaluate the long-term stability and adsorption performance of HBHC under conditions simulating acid-cleaning treatments in order to assess its durability in realistic industrial environments.

The Nyquist plots presented in Fig. 8a, illustrate the evolution of the metal's corrosion behavior over time in the absence of the HBHC corrosion inhibitor. All the curves display a single semicircle, which means the corrosion process is mainly controlled by charge transfer at the metal–solution interface. As the period of immersion increases from 1 day to 30 days, the sizes of the semicircles consistently decrease. This decrease indicates a gradual lowering of charge transfer resistance (R_{ct}), which implies that the metal is becoming more susceptible to corrosion. In other words, with longer exposure times, the metal

surface becomes increasingly reactive and more likely to corrode. The equivalent circuit used to fit the data, shown in the inset, includes a solution resistance (R_s) and a constant phase element (CPE_{dl}) parallel to R_{ct}. The use of a CPE instead of an ideal capacitor suggests some irregularity at the surface, likely due to surface roughness corrosion product accumulation, or uneven degradation.

When 200 ppm of HBHC inhibitor is present, the impedance values increase steadily up to 18 days, indicating the progressive formation and stabilization of the protective film. The slight variation observed between days 24 and 30 falls within the experimental margin of error and does not reflect a real decrease in protection. Overall, the impedance values remain stable at longer immersion times and are significantly higher than those of the uninhibited sample, confirming the durability and long-term protective effect of HBHC.

As shown in Fig. 8b, the impedance diagrams exhibit a similar shape at different immersion times, characterized by
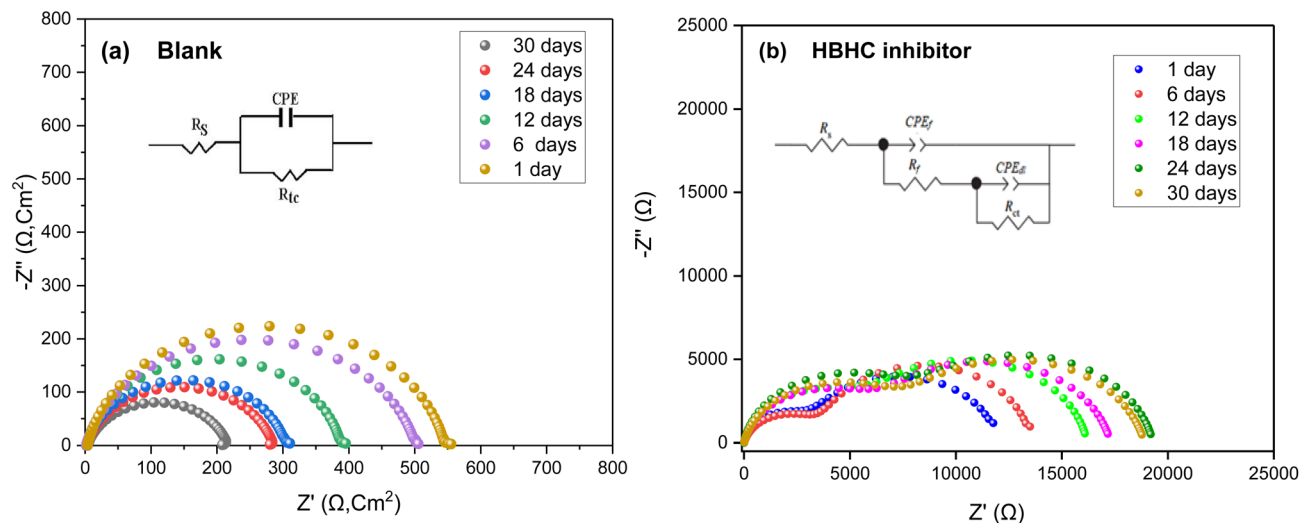
Fig. 8 Measured EIS response of the A179 steel samples immersed for 1, 6, 12, 18, 24, and 30 days in (a) 1 M HCl solution and (b) 1 M HCl solution containing 200 ppm of HBHC inhibitor at 298 K.

the appearance of two distinct loops. These correspond to two time constants: the high-frequency loop is related to the development of the inhibitor film, while the low-frequency loop is associated with charge transfer resistance. Over time, the capacitive loops expand, which is attributed to the adsorption of HBHC molecules on the steel surface, forming a protective barrier against corrosion.

The equivalent circuit model used to fit the impedance data is presented in the inset of Fig. 8b. The high-frequency loop is represented by a Constant Phase Element (CPE_f), simulating the non-ideal capacitance of the film, in parallel with the film resistance (R_f). The low-frequency loop corresponds to the double-layer Constant Phase Element (CPE_{dl}) in parallel with the charge transfer resistance (R_{ct}).

A comparison of the electrochemical impedance parameters is provided in Table 4 for steel samples immersed in the

corrosive medium with and without 200 ppm HBHC. In the absence of the inhibitor, the charge transfer resistance (R_{ct}) decreases markedly from 542.1 Ω cm^2 on day 1 to 212.2 Ω cm^2 on day 30, indicating a continuous increase in corrosion activity. In contrast, the presence of HBHC maintains much higher R_{ct} values, confirming its protective performance over prolonged exposure.

At the same time, the double layer capacitance (Q_{dl}) increases, suggesting a rise in the buildup of corrosion products and deterioration of the surface.

In contrast, when 200 ppm of HBHC is added, a substantial increase in both film resistance (R_f) and charge transfer R_{ct} is observed, with R_{ct} peaking at 9247.8 Ω cm^2 from day 1 to day 30. The lower Q_{dl} values and higher "n" factors (around 0.9) also indicate a more uniform and capacitive behavior, consistent with the presence of an effective barrier layer. This trend reflects

Table 4 Electrochemical impedance parameters of the corrosion of the A179 steel in 1 M HCl solution in the presence of 200 ppm of HBHC inhibitor at different immersion times

Time (days)	R_s (Ω cm^2)	CPE$_f$			R_f (Ω cm^2)	CPE$_{dl}$		R_{ct} (Ω cm^2)	IE (%)
		Q_f (F s^{n-1}) $\times 10^{-5}$	n			Q_{dl} (F s^{n-1}) $\times 10^{-6}$	n		
Blank									
1 day	2.22 ± 0.04	—	—	—	—	1.29 ± 0.05	0.878 ± 0.089	542.1 ± 98.2	—
6 days	1.58 ± 0.12	—	—	—	—	1.76 ± 0.11	0.854 ± 0.157	499.5 ± 87.5	—
12 days	1.14 ± 0.03	—	—	—	—	3.82 ± 0.09	0.888 ± 0.042	385.4 ± 112.3	—
18 days	2.85 ± 0.22	—	—	—	—	6.41 ± 0.06	0.865 ± 0.047	302.7 ± 103.3	—
24 days	3.05 ± 0.17	—	—	—	—	22.5 ± 0.08	0.834 ± 0.149	284.9 ± 85.7	—
30 days	2.87 ± 0.28	—	—	—	—	32.7 ± 0.07	0.824 ± 0.258	212.2 ± 45.2	—
200 ppm HBHC									
1 day	8.25 ± 0.15	2.32 ± 0.17	0.902 ± 0.05		9240.2 ± 125.8	2.54 ± 0.148	0.911 ± 0.047	2572.6 ± 225.1	78.92
6 days	7.55 ± 0.09	1.51 ± 0.24	0.944 ± 0.04		9895.1 ± 144.2	1.52 ± 0.097	0.865 ± 0.044	3645.4 ± 205.3	86.29
12 days	8.04 ± 1.05	0.762 ± 0.18	0.915 ± 0.02		10 540.6 ± 274.1	0.855 ± 0.284	0.922 ± 0.055	5542.1 ± 388.2	93.04
18 days	7.92 ± 0.08	0.514 ± 0.09	0.878 ± 0.05		11 433.3 ± 387.4	0.654 ± 0.254	0.887 ± 0.037	7445.9 ± 378.8	95.93
24 days	8.33 ± 0.16	0.454 ± 0.16	0.889 ± 0.01		11 040.3 ± 454.3	0.551 ± 0.015	0.898 ± 0.087	9247.8 ± 258.5	96.91
30 days	7.56 ± 1.12	0.478 ± 0.08	0.887 ± 0.02		10 899.5 ± 405.2	0.674 ± 0.087	0.881 ± 0.048	9025.7 ± 178.7	97.64

Table 5 Quantum chemical descriptors and reactivity indices calculated using DFT at the M06-2X/6-31G(d) level for the neutral and protonated forms of the HBHC molecule

Descriptor	Neutral HBHC	Protonated HBHC
Optimized energy (hartree)	−624.541	−624.973
E_{HOMO} (eV)	−7.327	−8.457
E_{LUMO} (eV)	−0.384	−2.063
Gap (HOMO–LUMO) (eV)	6943	6.394
I (eV)	7.327	8.457
A (eV)	0.384	2.063
η (eV)	3.472	3.197
χ (eV)	3.855	5.260
σ (eV)	0.288	0.313
ω (eV)	2.140	4.327
ε (eV)	0.467	0.231
$\Delta N_{110} = \dfrac{\chi_{Fe_{110}} - \chi_{inh}}{2(\eta_{Fe_{110}} + \eta)}$	0.139	−0.069

the gradual development of a stable and adherent film on the metal surface that limits charge transfer and thus reduces corrosion activity. The corresponding rise in inhibition efficiency (IE %), as illustrated in Table 5, from 87.92% to 97.64%, supports this interpretation and demonstrates that the HBHC compound offers an intense and persistent corrosion inhibition performance, suggesting its reliability for use in extended corrosive exposure.

3.5. Surface morphology assessment

3.5.1. Scanning electron microscopy (SEM) analysis. This research utilized scanning electron microscopy (SEM) to investigate the surface morphology and corrosion behavior of A179 MS exposed to 1 M HCl, with and without 200 ppm of HBHC inhibitor, over both short-term (1 day) and long-term (30 days) immersion periods.

The shiny coupons showed no significant flaws except for polishing scratches (Fig. 9a). In the case of HCl without inhibitor, the surface becomes noticeably damaged even after just one day (Fig. 9b) with clear signs of corrosion characterized by the existence of numerous corrosive pits distributed across the surface. After 30 days, the damage becomes much more severe. The surface of the A179 MS was strongly corroded with notable localized pits (Fig. 9c), which could be attributed to the corrosive effect of the 1 M HCl solution. When comparing Fig. 9b and c of MS in acidic medium without inhibitor to Fig. 9a of the polished MS, it is evident that the surface exhibits uniform corrosion accompanied by localized corrosion. On the other hand, the samples treated with 200 ppm of HBHC inhibitor show a stark contrast. Fig. 9d and e showed the changes in the surface appearance caused by the existence of a protective layer on the surface. After 1 day, the micrograph shows the absence of corrosion, and the surface remains relatively smooth and uniform, indicating that the protective film formed by the inhibitor is already active. Remarkably, even after 30 days of exposure, the inhibited surface still appears relatively intact and smooth, with only minimal changes.

The results demonstrate that the HBHC inhibitor efficiently adsorbs onto the A179 carbon steel surface, offering protective coverage. Therefore, the HBHC inhibitor not only reduces corrosion from the beginning but also offers continued protection to the material over extended exposure periods.

3.5.2. EDX analysis. To further, support our electrochemical findings that HBHC inhibits the corrosion of A179 carbon steel by forming a protective film on its surface, EDX spectra were recorded both in the absence and in the presence of HBHC at a concentration of 200 ppm. The elemental composition was determined using energy-dispersive X-ray spectroscopy (EDX). The EDX spectra in the Fig. 10 correspond to the surface composition of A179 MS after exposure to corrosive environments, both with and without a corrosion inhibitor (HBHC), for different immersion durations, 1 day and 30 days. Spectrum and map EDX (Fig. 10a) correspond to the sample immersed in 1 M HCl for 1 day. Here, the surface is composed mainly of iron (77.25 wt%), with minor amounts of oxygen (12.22 wt%), carbon (9.87 wt%), and chlorine (0.66 wt%), suggesting that the metal has just begun to react with the acidic environment, showing early signs of oxidation and slight chloride adsorption. In Fig. 10b, after 30 days in 1 M HCl without any inhibitor, the elemental composition changes drastically. Iron content falls sharply to 32.44 wt%, while oxygen and chlorine contents rise substantially to 34.22 wt% and 25.83 wt%, respectively; this change signifies a superficial alteration characterized by corrosion products, such as iron oxides and iron chlorides. The significant buildup of chlorine suggests a strong chloride assault, leading to considerable deterioration of the metal surface over time. Spectrum in Fig. 10c represents the condition after 1 day of immersion in 1 M HCl with 200 ppm of HBHC inhibitor. The iron content is even higher than in (a) and (b), at 79.23 wt%, and the chlorine level is lower at just 0.45 wt%, indicating that HBHC quickly adsorbs onto the metal surface, forming a protective layer that minimizes both oxidation and chloride penetration. The presence of nitrogen (2.69 wt%) and carbon (8.20 wt%) further supports the adsorption of the organic inhibitor onto the surface.[73] The oxygen (O) content was measured at 9.44 wt%. This relatively low concentration indicates minimal surface oxidation and limited formation of corrosion products, such as iron oxides or hydroxides. The reduction in oxygen content suggests that the existence of the inhibitor in the corrosive environment effectively suppressed the development of corrosion products on the steel substrate, as oxygen is a primary component in their formation.[74,75]

In the spectrum (Fig. 10d), the sample immersed for 30 days in the HCl with 200 ppm HBHC solution still shows a high iron content (77.73 wt%), indicating excellent long-term corrosion resistance. Nitrogen increases to 5.16 wt%, and carbon remains stable at 8.30 wt%, indicating that the inhibitor layer remains present and may even become more established over time. The oxygen content slightly drops to 8.53 wt%, and chlorine decreases further to 0.27 wt%, demonstrating continued suppression of both oxidation and chloride attack. Overall, the consistent carbon levels, rising nitrogen levels, and declining chlorine levels suggest that the HBHC inhibitor offers enduring
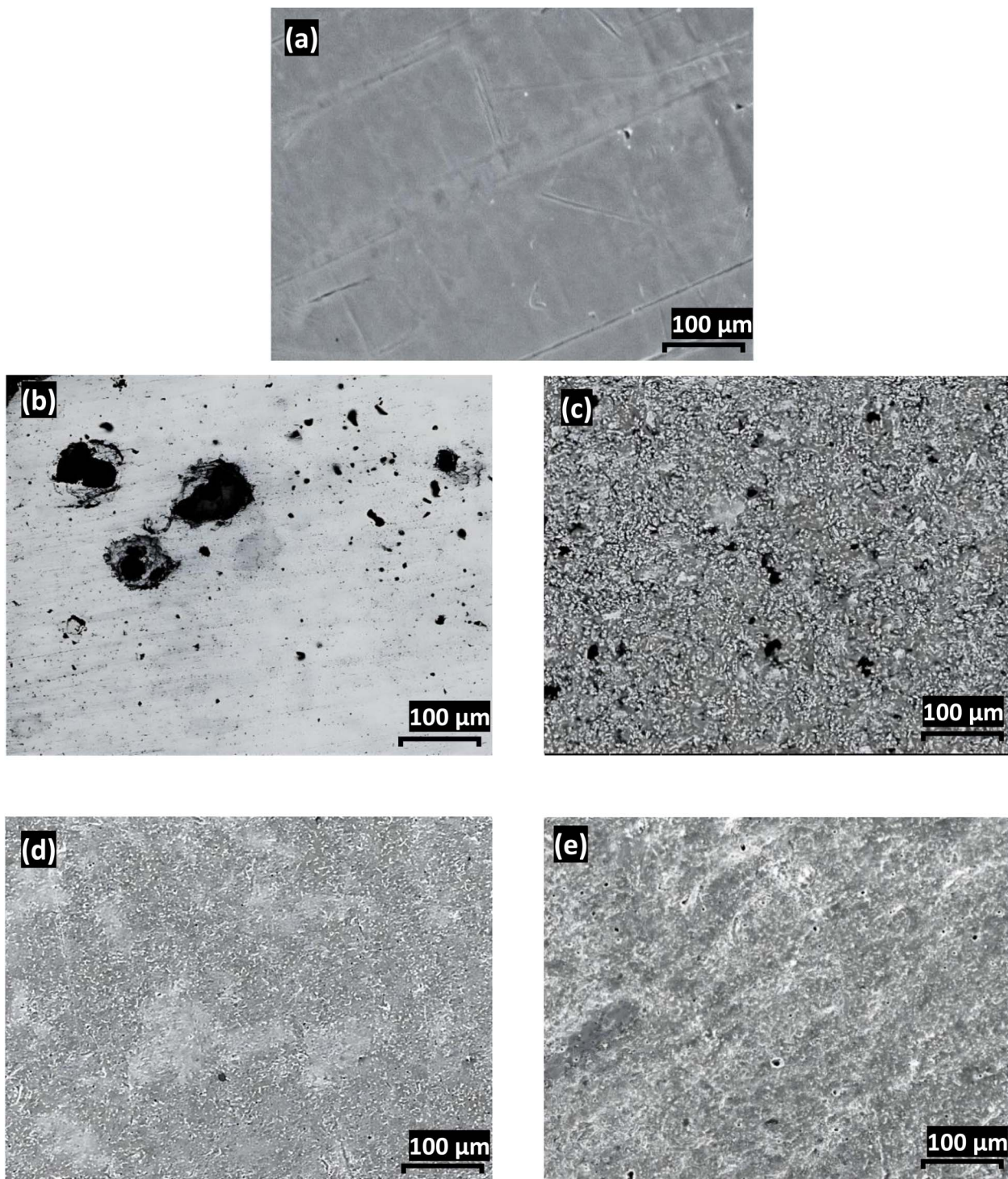
Fig. 9 SEM micrographs of A179 CS surface (a) sample freshly polished and immersed in (b) 1 M HCl for 1 day, (c) 1 M HCl for 30 days, (d) 1 M HCl in the presence of 200 ppm HBHC inhibitor for 1 day, and (e) 1 M HCl in the presence of 200 ppm HBHC inhibitor for 30 days.

protection by creating a stable and firmly adhering film on the metal surface, which substantially lowers corrosion during extended exposure.

3.6. Theoretical results

3.6.1. Prediction of the major microspecies (pK_a analysis). Organic inhibitors such as HBHC can undergo protonation and

deprotonation reactions at multiple ionizable sites depending on the pH of the environment, which significantly affects their inhibition efficiency. The distribution of HBHC protonation states as a function of pH was computed using MarvinSketch software,[76] as shown in Fig. 11.

At low pH values (below 3), the protonated species at the hydrazine nitrogen and the neutral form coexist in comparable
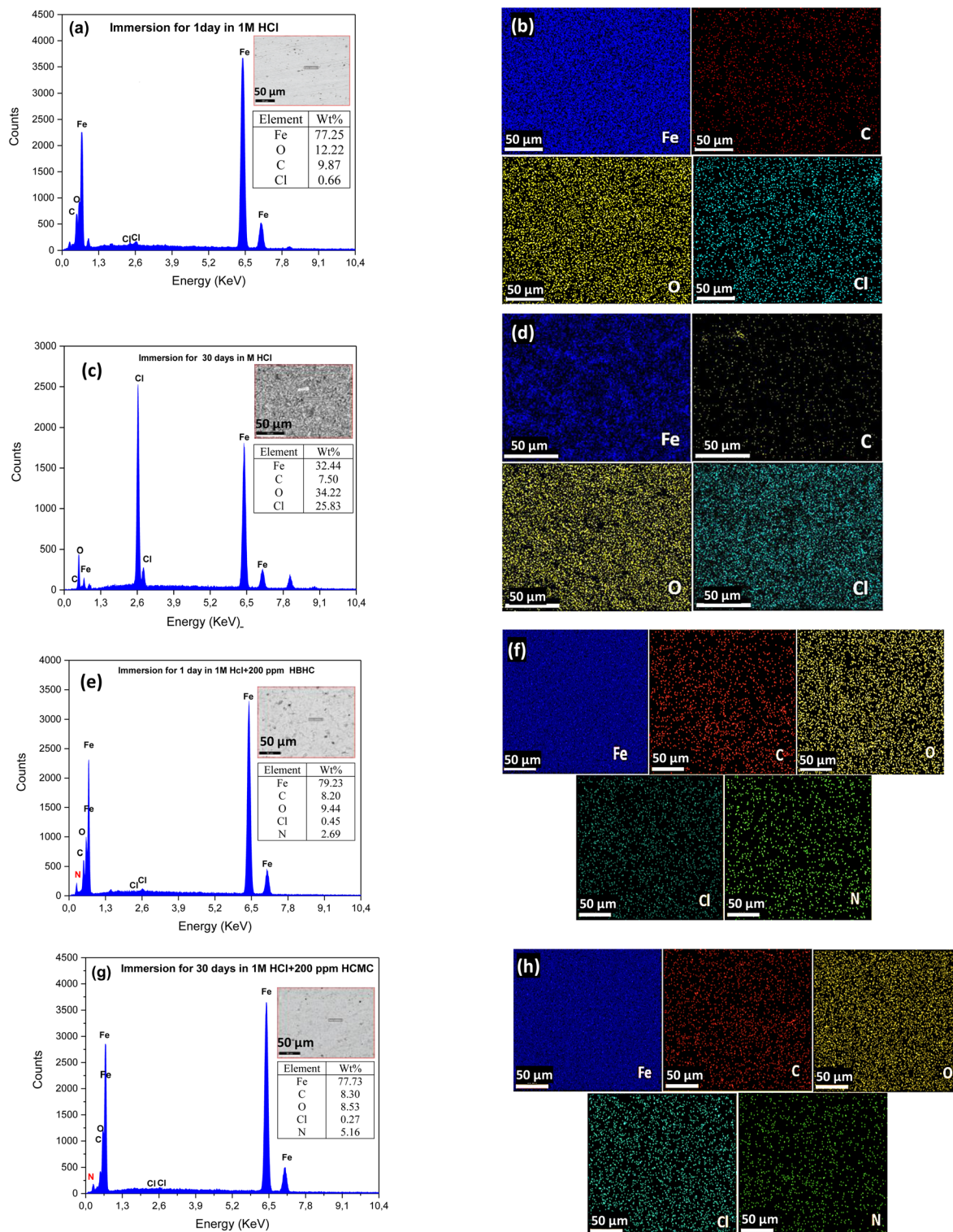
Fig. 10 EDX spectra and map EDX results of A179 CS surface immersed in (a and b) 1 M HCl for 1 day (c and d) 1 M HCl for 30 days (e and f) 1 M HCl with 200 ppm HBHC for 1 day (g and h) 1 M HCl with 200 ppm HBHC for 30 days at 298 K.

proportions rather than a single dominant species. This coexistence is evident in Fig. 11, where each species constitutes approximately 50% of the total distribution at around pH 1.08. Hence, the molecular population at acidic pH reflects a dynamic equilibrium between these two forms, affecting the adsorption characteristics and inhibitory performance.[77]

In the intermediate pH range (approximately 3 to 10), the neutral form becomes stabilized, partly due to intramolecular hydrogen bonding, and emerges as the predominant species. At
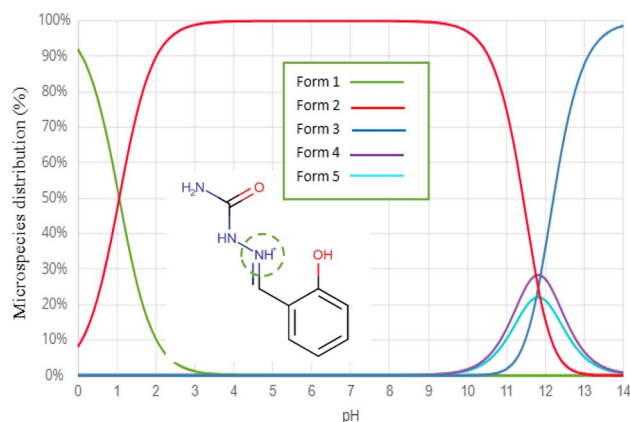
Fig. 11 Percentage distribution of different forms of HBHC as a function of pH, obtained by Marvin Sketch software.

alkaline pH values (above 11), both the phenolic hydroxyl (–OH) and the hydrazine nitrogen moieties undergo deprotonation in a narrow pH window, leading to the formation and coexistence of several anionic species. The overlapping protonation and deprotonation equilibria, due to closely spaced pK_a values of multiple functional groups in HBHC, result in the non-linear and complex distribution curves observed. This behavior is characteristic of polyfunctional organic molecules with multiple ionizable sites and reflects genuine chemical equilibria rather than random fluctuations. Additionally, the electronic properties and reactivity of the neutral and protonated forms were analyzed through optimized molecular structures and spatial distributions of HOMO and LUMO orbitals, providing insights into the protonation-dependent functionality of HBHC as a corrosion inhibitor.

3.6.2. DFT descriptors and frontier molecular orbitals. The electronic properties and reactivity of HBHC were analyzed for both the neutral and protonated forms. The optimized molecular structures and the spatial distributions of the HOMO and LUMO orbitals are presented in Fig. 12.

In the neutral form, the HOMO is primarily localized on nitrogen and oxygen atoms, indicating potential electron-donating sites, while the LUMO is distributed over the aromatic ring, suggesting electron-accepting regions. Upon protonation, significant changes in the localization of the frontier orbitals are observed, reflecting the altered electronic structure and reactivity.[78] The calculated quantum chemical descriptors are summarized in Table 5.

Table 5 presents the quantum chemical descriptors and reactivity indices for the HBHC molecule in both its neutral and protonated forms, calculated using DFT at the M06-2X/6-31G(d) level. The optimized energy of the protonated form (−624.973 hartree) is lower than that of the neutral form (−624.541 hartree), indicating that protonation leads to a more stable molecular structure. This increased stability may contribute to
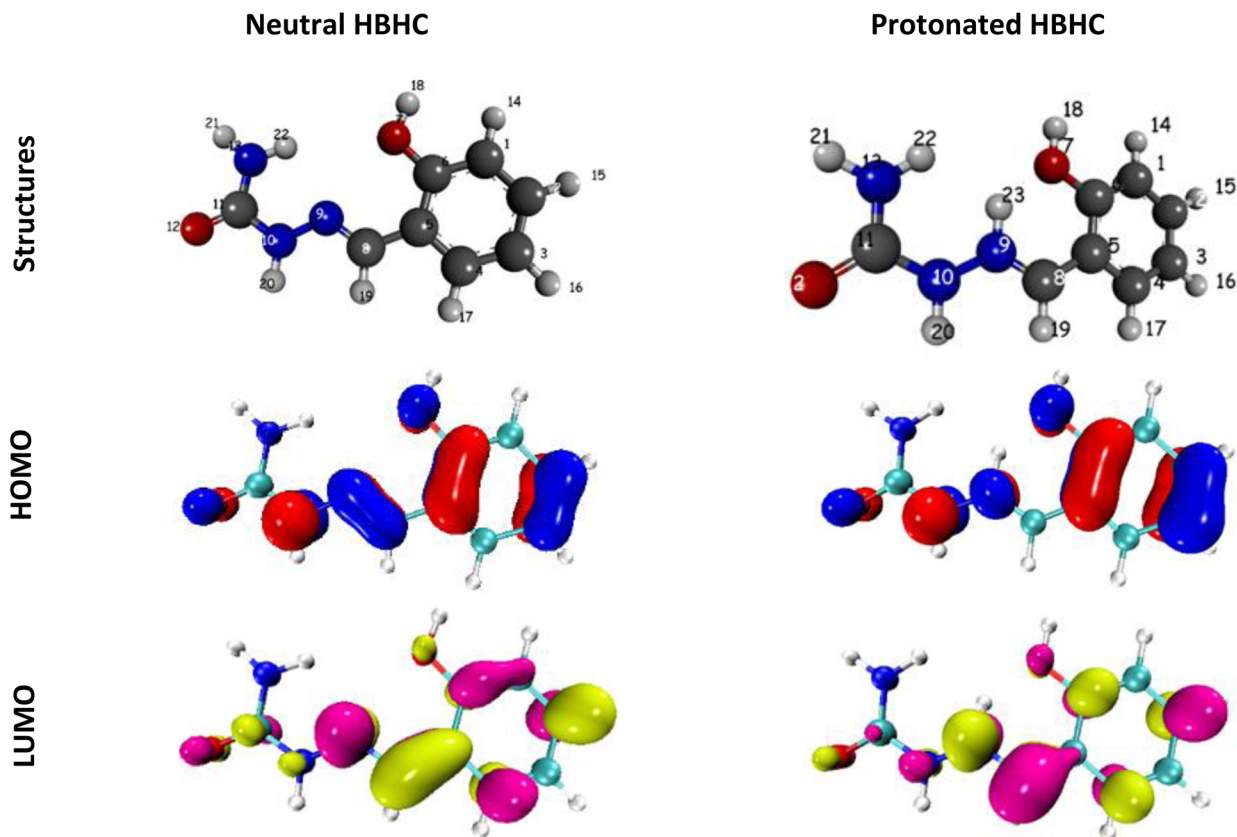

Fig. 12 Optimized geometry, HOMO, and LUMO orbitals of HBHC and HBHC$^+$ in their neutral and protonated forms in aqueous solution.

the enhanced persistence of the inhibitor under acidic conditions.[79]

The E_{HOMO} value, which reflects the ability of the molecule to donate electrons,[80] decreases from -7.327 eV in the neutral form to -8.457 eV in the protonated form. This decrease suggests that the protonated HBHC is less likely to act as an electron donor compared to the neutral form. Conversely, the E_{LUMO} value, which indicates the ability to accept electrons,[80] also decreases significantly from -0.384 eV (neutral) to -2.063 eV (protonated). This substantial reduction demonstrates that the protonated form is a much better electron acceptor.[80]

The HOMO–LUMO gap narrows from 6.943 eV in the neutral form to 6.394 eV in the protonated form, smaller HOMO–LUMO gap generally means higher chemical reactivity and greater ease of electron excitation, making the molecule more likely to participate in chemical interactions with the metal surface.[81] Regarding the ionization potential (I) and electron affinity (A), both parameters increase upon protonation (I: 7.327 → 8.457 eV; A: 0.384 → 2.063 eV). The higher ionization potential indicates that the protonated molecule is more resistant to losing electrons, while the increased electron affinity confirms its enhanced capacity to accept electrons.[82]

The chemical hardness (η) decreases slightly from 3.472 eV in the neutral form to 3.197 eV in the protonated form. Lower hardness is associated with higher reactivity, suggesting that the protonated HBHC is more chemically active and may interact more readily with the Fe(110) surface.[83] The electronegativity (χ) rises from 3.855 eV to 5.260 eV with protonation, reflecting a stronger tendency of the protonated form to attract electrons. This is further supported by the chemical potential (ε), which becomes more negative upon protonation (-3.855 → -5.260 eV), indicating a greater drive to acquire electrons from the environment.[84] The softness (σ), which is the inverse of hardness, increases from 0.288 eV (neutral) to 0.313 eV (protonated), reinforcing the observation that the protonated form is more reactive.[85] A notable increase is observed in the electrophilicity index (ω), which nearly doubles from 2.140 eV in the neutral form to 4.327 eV in the protonated form. This substantial rise demonstrates that the protonated HBHC is a much stronger electrophile, making it more effective at interacting with the electron-rich sites on the iron surface.[86] The electron transfer fraction (ΔN_{110}) changes from a positive value (0.139) in the neutral form to a negative value (-0.069) in the protonated form. A positive ΔN_{110} suggests electron transfer from the inhibitor to the metal, while a negative value indicates the reverse.[87] This shift implies that the direction and mechanism of charge transfer are affected by protonation, which could influence the adsorption mode and inhibition efficiency.[87]

These changes are expected to enhance the adsorption of the protonated molecule onto the Fe(110) surface, consequently improving its performance as a corrosion inhibitor, especially in acidic environments where protonated species predominate.

Importantly, these theoretical descriptors correlate well with the experimental inhibition trends. The relatively high E_{HOMO} of the neutral form supports moderate inhibition efficiencies under near-neutral conditions, where electron donation from

HBHC to Fe is favored. In contrast, the protonated form exhibits a much lower E_{LUMO}, narrower energy gap, and higher electrophilicity index, all of which enhance its ability to accept electron density from the Fe surface via back-donation. This dual charge-transfer pathway, as reflected in the change of ΔN from positive to negative values, explains the stronger and more stable adsorption of protonated HBHC observed experimentally, and hence its superior inhibition performance in acidic environments.

3.6.3. Fukui functions and electrostatic potential mapping. Fukui functions, charge density difference, and ESP maps were used to identify the key reactive sites and visualize local reactivity patterns. These analyses clarify the preferred adsorption regions and electronic changes upon protonation (see Table 6 and Fig. 13). As shown in Table 6, N(10) and O(12) in the neutral HBHC molecule exhibit the highest nucleophilic character ($f^- =$ 0.1171 and 0.1065), making them likely sites for electron donation. In contrast, N(9) displays the strongest electrophilic behavior ($f^+ = 0.1192$). Upon protonation, all key atoms (N(9), C(2), O(12)) display strong electrophilic behavior (f^+ values up to 0.1105) and positive CDD values, indicating increased electron-accepting ability.[88] As illustrated in Fig. 13, the ESP maps highlight the redistribution of electron density, with nucleophilic regions concentrated around N(10) and O(12) in the neutral form and enhanced positive potential around N(9) and C(2) in the protonated form. These findings indicate that protonation enhances the molecule's capacity to interact with the Fe(110) surface through its electrophilic centers, supporting a mechanism of strong and selective adsorption. Such behavior is beneficial for corrosion inhibition in acidic environments and is consistent with trends reported for similar organic inhibitors.[77]

3.6.4. Monte Carlo simulations. Monte Carlo simulations were performed to investigate the adsorption behavior of HBHC on the Fe(110) surface. The key results obtained from these simulations are summarized in Table 7. Monte Carlo simulations indicate strong adsorption of both neutral and protonated HBHC on Fe(110). The total energy is lower for the protonated form (-349.5307 kcal mol^{-1}) than for the neutral form (-333.2248 kcal mol^{-1}), reflecting greater stability.

Both forms exhibit highly negative adsorption energies (HBHC: -1698.6080 kcal mol^{-1}; HBHC$^+$: -1688.5220 kcal mol^{-1}), confirming strong surface binding. The neutral form exhibits a more negative rigid adsorption energy (-169.2090 kcal mol^{-1}), indicating a stronger initial interaction with the surface. In contrast, the protonated form

Table 6 Fukui functions and Charge Density Difference (CDD) values for selected atoms in neutral and protonated HBHC

Molecule	Atom	f^- (Nucleophilic)	f^+ (Electrophilic)	CDD
HBHC	N(10)	0.1171	0.0272	-0.0899
	O(12)	0.1065	0.0687	-0.0378
	N(9)	0.0577	0.1192	0.0614
HBHC$^+$	N(9)	-0.1951	0.1105	0.3056
	C(2)	-0.1971	0.0875	0.2847
	O(12)	-0.1386	0.0694	0.2079

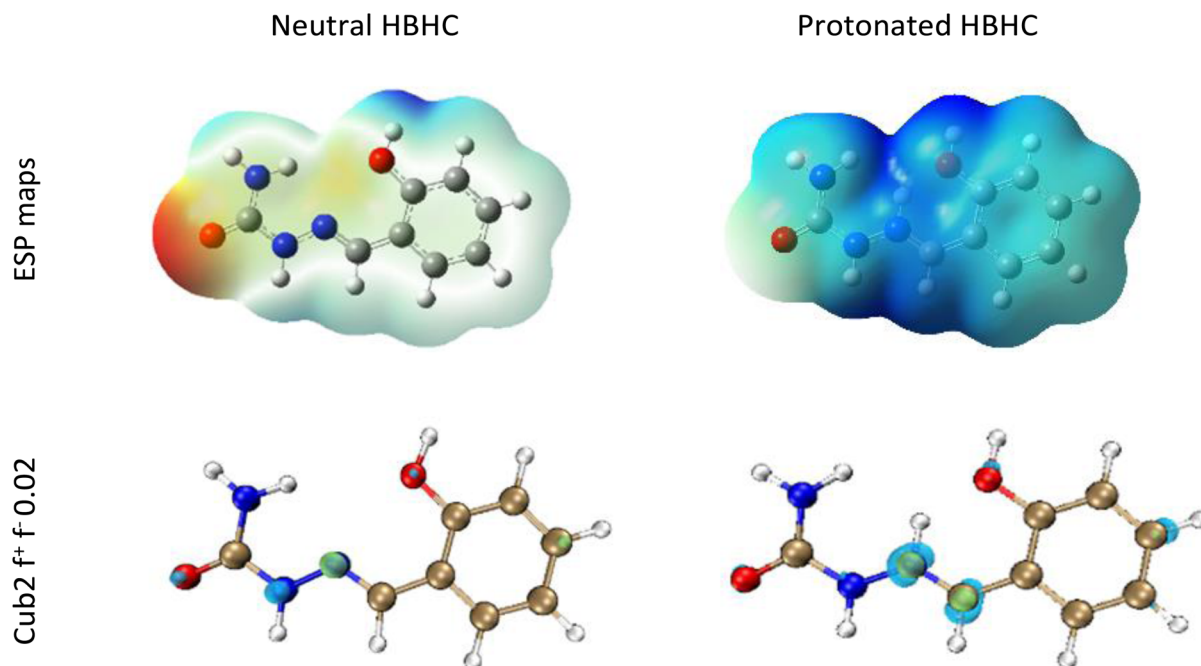

Neutral HBHC

Protonated HBHC

Fig. 13 Electrostatic potential (ESP) maps and Fukui function distributions (f^+ and f^-) for the neutral and protonated forms of HBHC.

Table 7 Monte Carlo energetic parameters for neutral and protonated HBHC on Fe(110) surface (kcal mol^{-1})

Structures	Total energy	Adsorption energy	Rigid adsorption energy	Deformation energy	dE_{ad}/dN_i
HBHC	−333.225	−1698.608	−169.209	−1529.399	−1698.608
HBHC$^+$	−349.531	−1688.522	−109.009	−1579.513	−1688.522

displays a significantly higher deformation energy (−1579.5130 kcal mol^{-1}), suggesting greater structural adjustment upon adsorption.[89] These findings indicate that both forms possess high affinity and adaptability toward the surface, with the protonated species demonstrating a particularly pronounced ability to accommodate structural changes during adsorption.

3.6.5. Molecular dynamics (MD) simulations. Molecular dynamics simulations were performed to investigate the adsorption configurations and stability of neutral and protonated HBHC molecules on the Fe(110) surface. Fig. 14 shows the top and side views of the most stable adsorption configurations for both forms. Both neutral and protonated HBHC adopt a nearly parallel orientation relative to the Fe(110) surface, maximizing contact and favoring strong adsorption. The slight differences in geometry between the two species reflect the influence of protonation on their interaction with the iron substrate. The calculated adsorption energies confirm strong interactions, with both molecules adopting nearly parallel orientations that maximize their contact with the metal surface.

The distances between the main reactive atoms of HBHC and the Fe(110) surface, summarized in Table 8, further clarify the adsorption behavior. For the protonated form, the Fe–N(9) distance is reduced to 2.932 Å compared to 3.144 Å for Fe–N(10)

in the neutral form, indicating stronger and more direct interaction. Similarly, Fe–C(2) and Fe–O(12) distances are slightly shorter or comparable in the protonated form, supporting the observation of enhanced adsorption. These results are consistent with previous studies, which have shown that protonation enhances the adsorption and inhibitory performance of organic inhibitors on metal surfaces by increasing their electrophilicity and interaction strength.[89–91]

3.6.6. Noncovalent interaction study. The Non-Covalent Interaction (NCI) analysis, as illustrated in Fig. 15, offers a comprehensive visualization of the weak intermolecular forces governing the adsorption of HBHC inhibitors, both in their neutral and protonated forms, on the carbon steel surface. The color-coded RDG isosurfaces and scatter plots distinctly characterize the nature and intensity of these interactions within the system.

In the neutral HBHC structure, the RDG scatter plot reveals prominent blue regions at sign(λ_2)ρ values around −0.020 a.u., corresponding to strong hydrogen bonding interactions. These are predominantly localized near the nitrogen and oxygen atoms, with RDG values peaking at approximately 1.5, indicating significant stabilization through hydrogen bonding.

Green regions, centered near sign(λ_2)ρ = 0 a.u. and RDG values between 0.5 and 1.2, reflect the presence of van der Waals
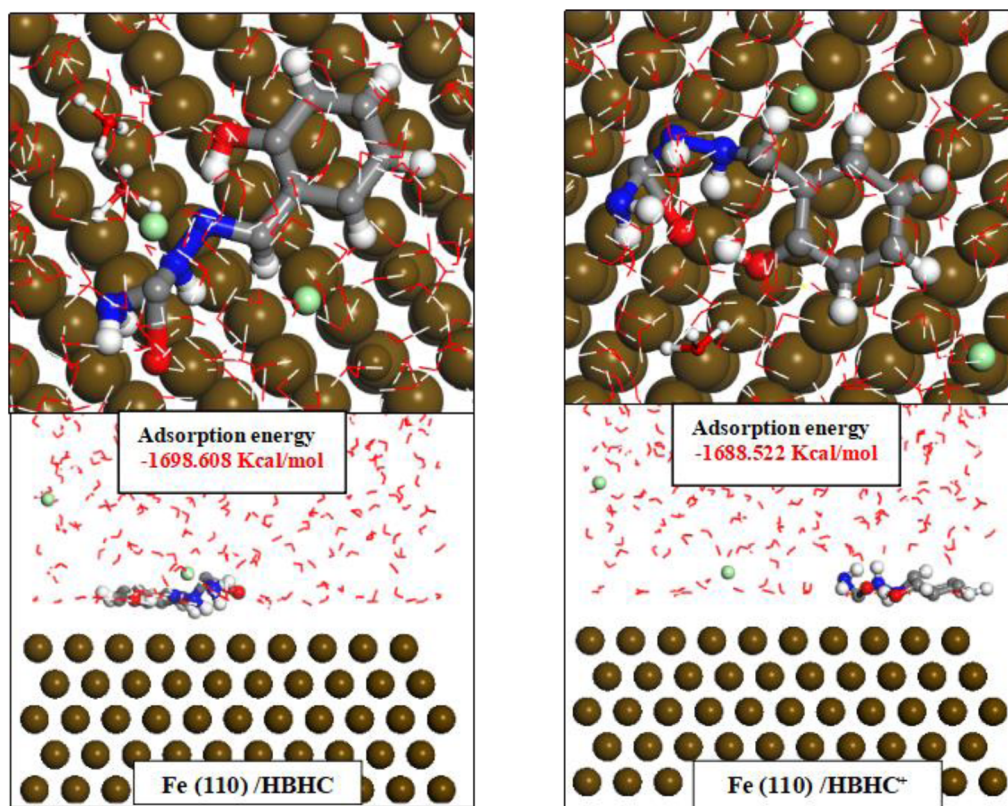
Fig. 14 Adsorption geometries of neutral and protonated HBHC on Fe(110) surface: top and side perspectives from MD simulations.

Table 8 Distances between key reactive atoms of protonated (HBHC$^+$) and non-protonated (HBHC) inhibitor molecules and Fe atoms on the Fe(110) surface

Molecule	Fe/atom pair	Distance (Å)
HBHC	Fe/N(10)	3.144
	Fe/O(12)	3.564
	Fe/N(9)	3.328
	Fe/C(2)	3.208
HBHC$^+$	Fe/N(9)	2.932
	Fe/C(2)	3.195
	Fe/O(12)	3.625

forces, particularly across the aromatic rings and methoxy groups.

Red regions, observed at positive sign(λ_2)ρ values up to 0.020 a.u., signify steric repulsion, but their relatively limited intensity (RDG < 0.5) suggests that the molecular geometry of HBHC efficiently mitigates unfavorable crowding at the interface.

Upon protonation, the HBHC molecule exhibits an intensification of blue regions in the RDG plot, with sign(λ_2)ρ values extending to −0.025 a.u. and RDG maxima approaching 1.8. This enhancement indicates stronger and more numerous hydrogen bonds, especially around the protonated nitrogen centers, which act as effective electrophilic sites for interaction with the electron-rich steel surface.[91] The green van der Waals regions remain well distributed, supporting stable adsorption,

while the red steric repulsion zones do not increase significantly, confirming that protonation does not introduce substantial spatial hindrance. Quantitatively, the RDG isovalue range from −0.035 to 0.020 a.u. across both forms of HBHC demonstrates a balanced interplay between attractive and repulsive interactions. The predominance of blue and green regions, coupled with the limited presence of red, underscores the favorable adsorption profile of HBHC, ensuring robust surface coverage and effective inhibition of corrosive species. The analysis confirms that both neutral and protonated HBHC molecules form stable, protective layers on carbon steel by maximizing hydrogen bonding and van der Waals interactions while minimizing steric repulsion. The protonated form, in particular, enhances adsorption strength, which is advantageous for corrosion inhibition in acidic environments. These findings are consistent with the observed trends in the RDG plots and support the molecular design principles for efficient organic corrosion inhibitors.

3.7. Proposed inhibitory mechanism

The illustrated mechanism presented in Fig. 16 represents the adsorption behavior of the inhibitor HBHC onto an iron surface (Fe^{2+}/Fe^{3+}), showing both neutral and protonated forms of the molecule. Two main processes govern the interaction of HBHC with the metal surface: chemical adsorption (chemisorption) and physical adsorption (physisorption). Chemical adsorption of HBHC on the metal surface occurs mainly through electron
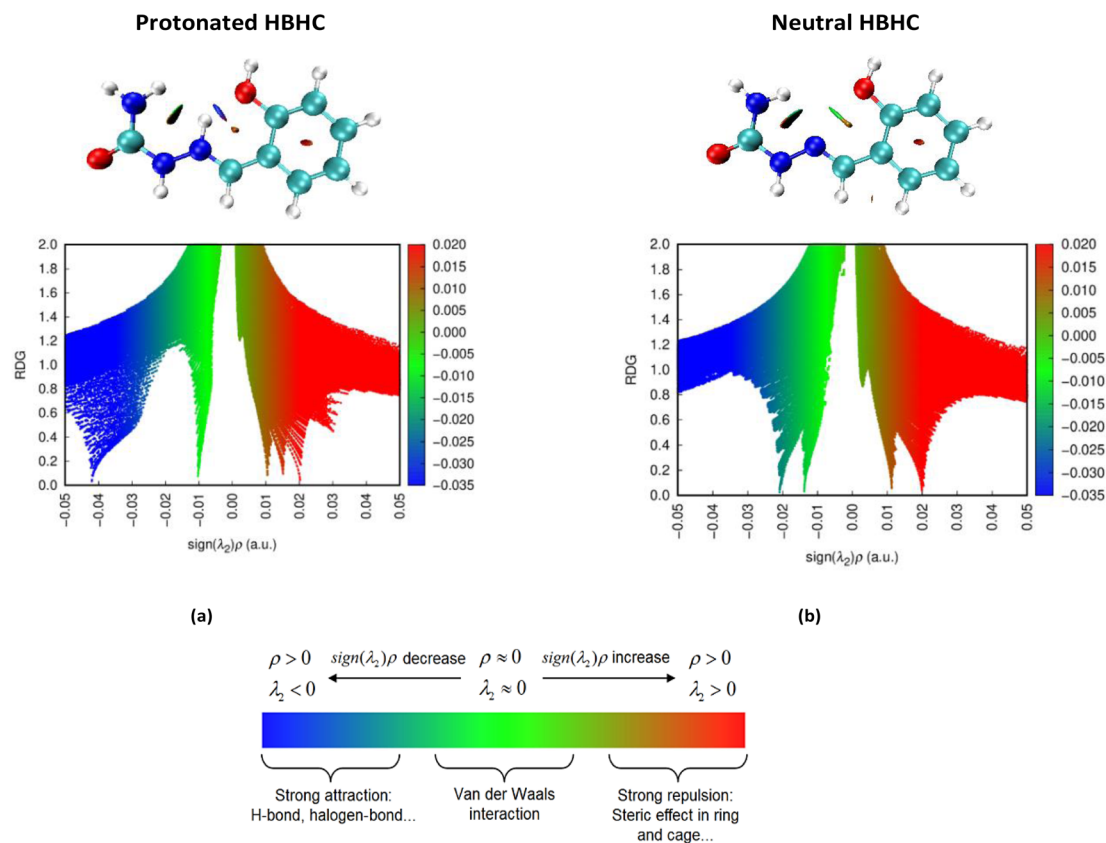
Protonated HBHC

Neutral HBHC

Fig. 15 Comparative NCI (RDG) isosurfaces and scatter plots for (a) protonated and (b) neutral HBHC inhibitors.
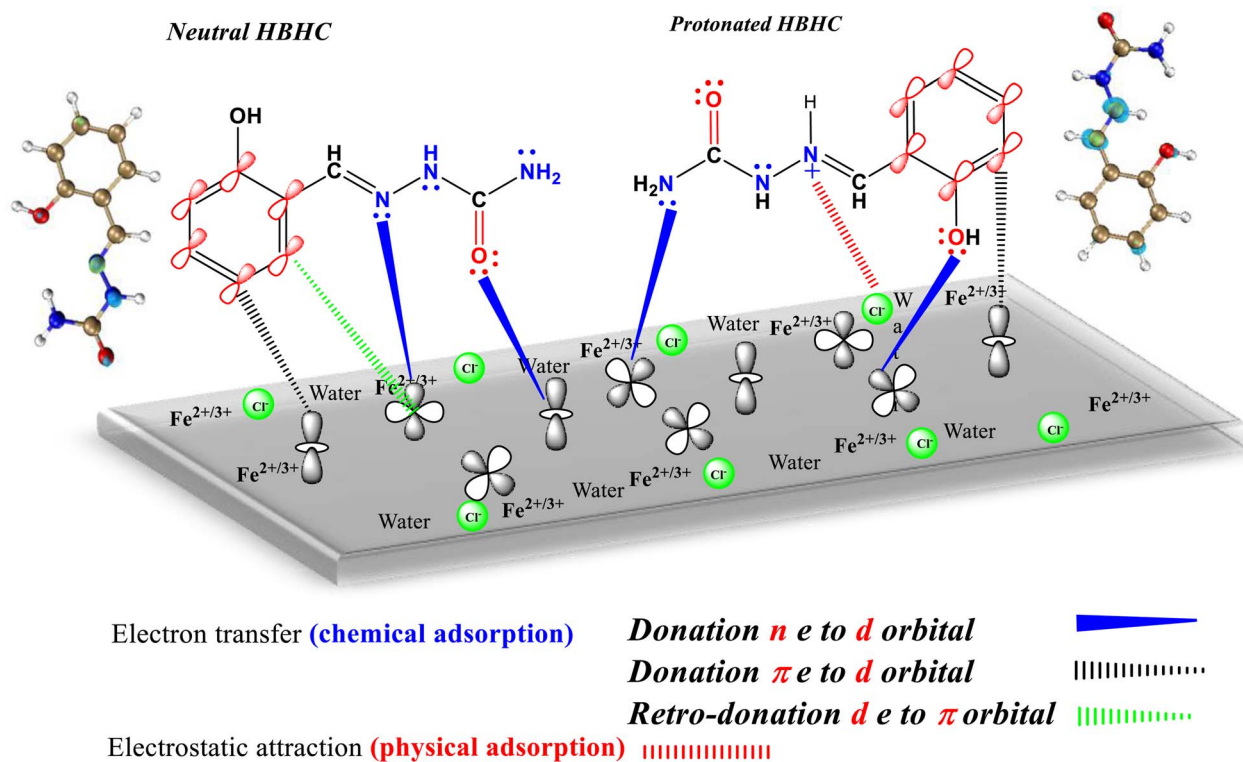

Fig. 16 Proposed adsorption and protection mechanism of metal surface in acidic media.

transfer interactions between electron-rich atoms or groups in the HBHC molecule and the d-orbitals of iron (Fe) atoms. First, lone pair electrons (n) from heteroatoms such as nitrogen (found in –NH–NH– groups and amide functionalities) and oxygen (from hydroxyl and carbonyl groups) donate electron density to the vacant Fe d-orbitals (n → d), represented by solid blue arrows. Second, the delocalized π-electrons of the aromatic benzene rings interact with the Fe surface by donating electron density to the metal d-orbitals (π → d), illustrated by dashed black lines, through mechanisms such as π-backbonding or π-complex formation.

Finally, there is a retro-donation process where electrons from the Fe d-orbitals are back donated into the π* antibonding orbitals of HBHC (d → π*), shown as dashed green lines, which further stabilizes the metal–inhibitor complex by strengthening the interaction with a partial covalent character. On the other hand, physical adsorption involves electrostatic attractions between the positively charged Fe^{2+}/Fe^{3+} ions on the metal surface and the negatively charged or Polar regions of the inhibitor, such as lone pair-bearing atoms or deprotonated groups. Red dashed lines depict these interactions. Although weaker than chemisorption, physisorption can facilitate initial binding, especially in the early stages of inhibition. The diagram clearly distinguishes the adsorption behavior in the neutral *versus* protonated forms of HBHC. Protonation enhances the electron-withdrawing character of the molecule, often increasing the molecule's dipole moment and solubility in acidic environments (such as 1 M HCl), thereby improving its adsorption efficiency.

In the protonated form, new sites become positively charged, promoting stronger electrostatic interactions with the metal surface and possibly improving hydrogen bonding with adsorbed water molecules. Overall, this dual adsorption mechanism, involving both donor–acceptor interactions (chemisorption) and electrostatic forces (physisorption), enables HBHC to form a stable protective layer on the iron surface. This layer effectively isolates the metal from the corrosive environment, reducing both anodic and cathodic reactions and confirming HBHC's

potential as a high-performance corrosion inhibitor in acidic media.

3.8. ADMET analysis for HBHC corrosion inhibition

The pharmacokinetic, toxicity, and operational properties of HBHC and its protonated form ($HBHC^+$) were predicted using ADMETlab 2.0.[92] The main descriptors, including lipophilicity (log P), solubility, bioavailability, plasma protein binding, membrane permeability, and potential toxicity risks, are summarized in Table 9 and S1. Both HBHC and $HBHC^+$ exhibit log P values within the optimal range (0–3), indicating favorable lipophilicity, and predicted topological polar surface area (TPSA < 140 Å^2) and Caco-2 permeability values suggest acceptable membrane permeability. However, the human intestinal absorption (HIA) probabilities remain low, indicating limited oral absorption.

Regarding systemic distribution, both molecules display high plasma protein binding (>90%) and a strong likelihood of blood–brain barrier penetration. Predicted clearance rates (7.5–8.5 mL min^{-1} kg^{-1}) indicate moderate elimination. In terms of toxicity, HBHC and $HBHC^+$ show potential risks of mutagenicity (Ames positive probability ~0.4), drug-induced liver injury (DILI), and skin sensitization, while hepatotoxicity and carcinogenicity probabilities are relatively low. Both compounds also show low predicted human toxicity overall, supporting worker safety and suitability for industrial use.

From an environmental and operational perspective, HBHC and $HBHC^+$ demonstrate good water solubility (log S between −2 and −3), chemical stability under operational conditions, and low bioaccumulation, ensuring effective dispersion, uniform metal surface coverage, long-term corrosion protection, and minimal long-term environmental impact.[93,94] $HBHC^+$ exhibits slightly lower aquatic toxicity and bioaccumulation, making it more environmentally favorable in contexts where discharge into water systems is possible.

Overall, the ADMET predictions indicate that HBHC and $HBHC^+$ possess drug-like physicochemical profiles, moderate bioavailability, and acceptable safety margins, with certain
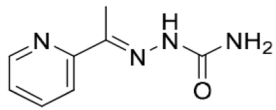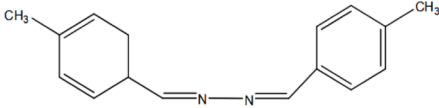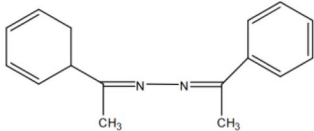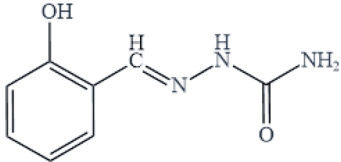
Table 9 Key ADMET-related properties for HBHC and HBHC$^{+a,b,c,d,e}$

Property	HBHC	HBHC$^+$
Human toxicity	Low	Low
	Hepatotoxicity: 0.029	Hepatotoxicity: 0.033
	DILI: 0.77	DILI: 0.913
	Ames: 0.417	Ames: 0.407
Aquatic toxicity	Moderate	Low
	Bioaccumulation: 0.586, LC50FM: 4.58, LC50DM: 4.318	Bioaccumulation: 0.593 LC50FM: 4.474, LC50DM: 4.316
Water solubility (log S)	Good (−2.748)	Good (−2.945)
Chemical stability	High	High
	Stable under operational conditions, no instability alerts	Stable under operational conditions, no instability alerts
Bioaccumulation	Low	Low
	Bioaccumulation factor: 0.586	Bioaccumulation factor: 0.593

[a] DILI: Drug-Induced Liver Injury. [b] Ames: Ames Mutagenicity Test. [c] LC50FM: Lethal Concentration 50% – Fathead Minnow. [d] LC50DM: Lethal Concentration 50% – Daphnia magna. [e] log S: Logarithm of Aqueous Solubility.

Table 10 Comparative analysis of corrosion inhibition efficiency of HBHC in comparison to selected literature findings

Inhibitor	Metal/alloy	Solution	IE (%)	Ref.
(E)-2-(1-Triazylidineethyl)pyridine	Mild steel	1 M HCL	77.7% PDP 87.29% EIS	94
1-(4-Methylbenzylidene)-2-((4-methylcyclohexa-2,4-dienyl)methylene)hydrazine	Stainless steel	1 M HCl	86.6% PDP 86.2% EIS	25
1-(1-(Cyclohexa-2,4dienyl)ethylidene)-2-(1-phenylethylidene)hydrazine	Stainless steel	1 M HCl	86.3% PDP 85.2% EIS	95
(E)-2-((2-Hydroxybenzylidene))hydrazine-1-carboxamide	Mild steel	1 M HCL	94.5% PDP 93.33% EIS	This work

toxicity alerts (DILI, skin sensitization) that require further experimental validation. Both compounds meet key criteria for operational performance, worker safety, and environmental protection, making them effective, stable, and safe corrosion inhibitors for industrial applications, with HBHC[+] preferred in environmentally sensitive contexts.

3.9. Comparative analysis with literature data

In our study, we evaluated the corrosion inhibition efficiency of HBHC against results reported in the literature, as presented in Table 10. This comparison provides insight into HBHC's performance relative to other established inhibitors and underscores its distinctive characteristics as a corrosion inhibitor for mild steel. HBHC demonstrates excellent corrosion resistance, as confirmed by different tests such as PDP and EIS analyses. Its corrosion inhibition efficiency varies between 93.33% (EIS) and 94.50% (PDP), depending on the specific method and experimental conditions applied. When compared with previous studies, HBHC exhibits equal or superior effectiveness in mitigating corrosion. For instance, it performs better than (E)-2-(1-triazylidineethyl) pyridine for protecting carbon and mild steel in 1 M HCl.[95] It also surpasses 1-(4-methylbenzylidene)-2-(4-methylcyclohexa-2,4-dienyl methylene)

hydrazine[25] and 1-(1-(cyclohexa-2,4-dienyl) ethylidene) 2-(1-phenylethylidene) hydrazine[96] for protecting stainless steel in 1 M HCl in electrochemical tests, confirming its high efficiency and adaptability under acidic conditions. This comparison highlights HBHC's competitive advantage and its valuable contribution to corrosion inhibition research. The promising results encourage further research into HBHC for corrosion mitigation, paving the way for new, effective industrial applications.

4. Conclusion

This study demonstrates the strong anticorrosion performance of (E)-2-((2-hydroxybenzylidene)) hydrazine-1-carboxamide (HBHC) as a novel inhibitor for A179 steel in 1 M HCl. Electrochemical measurements confirmed its optimal efficiency at 200 ppm, with inhibition efficiencies above 93%, and revealed its mixed-type inhibition behavior. Adsorption followed the Langmuir isotherm, involving both physical and chemical interactions through heteroatoms. Long-term immersion tests further highlighted the stability of the protective film, with efficiency increasing up to 97.6% after 30 days. Surface analyses (SEM-EDX) verified the formation of a uniform protective layer, while theoretical studies (DFT and molecular

dynamics) supported the strong affinity of HBHC and its protonated form toward the steel surface. Moreover, ADMET analysis confirmed its favorable safety and environmental profile.

The promising anticorrosion performance of HBHC underscores its potential for practical applications in acidic environments. Its high efficiency at low concentrations and long-term stability make it suitable for protecting steel pipelines and equipment in oil and gas industries, as well as in chemical processing systems. Furthermore, its favorable ADMET profile suggests that HBHC can serve as a safer and more sustainable alternative to conventional toxic inhibitors.

Author contributions

Hind Boughazi: writing and drafting of the manuscript, experimental investigation, discussion of results. Yamina Boudinar: supervision, formal analysis, data curation. Samira Tlihi: experimental investigation (MEB/EDX), validation of results. Amel Djedouani: manuscript revision. Noura Naili: computational studies (DFT, MarvinSketch, ADMET), discussion of results, editing and writing.

Conflicts of interest

There are no conflicts to declare.

Data availability

The datasets supporting the findings of this study are available from the corresponding author upon reasonable request.

Supplementary information (SI): additional results on predicted quantitative ADMET properties of HBHC and its protonated form (HBHC$^+$). See DOI: https://doi.org/10.1039/d5ra05876g.

Acknowledgements

References

1 R. E. Malchers, *npj Mater. Degrad.*, 2019, **3**, 4.

2 C. Nyby, X. Guo, J. E. Saal, S.-C. Chien, A. Y. Gerard, H. Ke, T. Li, P. Lu, C. Oberdorfer, S. Sahu, S. Li, C. D. Taylor, W. Windl, J. R. Scully and G. S. Frankel, *Sci. Data*, 2018, **8**, 58.

3 K. Muthamma, P. Kumari, M. Lavanya and S. A. Rao, *J. Bio Tribo Corros.*, 2021, **7**(8), 10.

4 A. Guendouz, W. Ettahiri, M. Adardour, J. Lazrak, E. H. E. Assiri, A. Taleb, B. Hammouti, Z. Rais, A. Baouid and M. Taleb, *J. Mol. Struct.*, 2025, **1321**, 139901.

5 M. Wasim and M. B. Djukic, *J. Nat. Gas Sci. Eng.*, 2022, **100**, 104467.

6 L. Xu, Y. Wang, L. Mo, Y. Tang, F. Wang and C. Li, *Eng. Fail. Anal.*, 2023, **144**, 106951.

7 W. Wang, W. Mu, M. Han, Y. Zhang, N. Wang, W. Zhang, Z. Li, Z. Weng and P. K. Liaw, *Mater. Des.*, 2025, **256**, 114230.

8 X. Liu, Z. Ma, C. Yang, X. Li, J. Yang, H. Ren and H. Ma, *J. Rare Earths*, 2025, **43**, 1758–1768.

9 Z. Shi, C. Fang, J. Li, S. Bandaru, M. Liu, L. Zhao and X. Zhang, *Small*, 2025, **21**, 2500629.

10 Y. Liu, L. Zhu, G. Ma, Y. Lu, A. Wei, C. Yang, Y. Huang, M. Liu and H. Wang, *Corros. Sci.*, 2025, **256**, 113221.

11 A. Al-Amiery, W. N. R. Wan Isahak and W. K. Al-Azzawi, *Ain Shams Eng. J.*, 2024, **15**, 102672.

12 R. O. Medupin, K. O. Ukoba, K. O. Yoro and T.-C. Jen, *Mater. Today Sustainability*, 2023, **22**, 100373.

13 A. A. Al-Amiery, W. N. R. W. Isahak and W. K. Al-Azzawi, *Lubricants*, 2023, **11**, 174.

14 Y. P. Asmara, F. Herlina and A. G. E. Sutjipto, *Defect Diffus. Forum*, 2024, **431**, 69–76.

15 Z. Shang and J. Zhu, *J. Mater. Res. Technol.*, 2021, **15**, 5078–5094.

16 L. A. Khaleel, O. A. Hatem and D. A. Alwan, *Results Chem.*, 2025, **15**, 102160.

17 P. Singaravelu, N. Bhadusha and V. Dharmalingam, *Int. J. Life Sci. Pharma Res.*, 2022, L40–L50.

18 M. Azogagh, A. El Magri, R. Hsissou, R. Lachhab, K. P. Katin, E. Berdimurodov, M. Galai, S. E. Hegazi and M. Rafik, *J. Mol. Liq.*, 2024, **416**, 126459.

19 N. Benachour, A. Delimi, H. Allal, A. Boublia, A. Sedik, H. Ferkous, A. Djedouani, S. Brioua, C. Boulechfar, H. Benzouid, A. Houssou, A. Oral, B. Ernst, M. Alam and Y. Benguerba, *RSC Adv.*, 2024, **14**, 12533–12555.

20 A. Belkheiri, K. Dahmani, K. Mzioud, M. Khattabi, O. Kharbouch, M. Galai, Y. Merroun, N. Dkhireche, Z. Benzekri, S. Boukhris, R. Almeer, A. Chaouiki and M. E. Touhami, *Int. J. Electrochem. Sci.*, 2025, **20**, 100907.

21 H. S. Abood, E. Q. Jasim and M. A. Muhammad-Ali, *Sci. Technol. Indones.*, 2024, **9**, 137–147.

22 H. A. Batakoushy, S. A. Abouel-Enein, R. M. M. Morsi, H. M. Awad, B. Ghazal and H. S. Mandour, *Sci. Rep.*, 2024, **14**, 21138.

23 M. El Azzouzi, A. Aouniti, S. Tighadouin, H. Elmsellem, S. Radi, B. Hammouti, A. El Assyry, F. Bentiss and A. Zarrouk, *J. Mol. Liq.*, 2016, **221**, 633–641.

24 P. Preethi Kumari, P. Shetty and S. A. Rao, *Arab. J. Chem.*, 2017, **10**, 653–663.

25 A. S. Fouda, S. A. AbdEl-Maksoud, A. El-Hossiany and A. Ibrahim, *Int. J. Electrochem. Sci.*, 2019, **14**, 2187–2207.

26 H. M. Gebremeskel, M. A. Welearegay and T. T. Nadew, *Quantum Eng.*, 2024, **2024**, 5343086.

27 M. E. Belghiti, M. Mihit, A. Mahsoune, A. Elmelouky, R. Mghaiouini, A. Barhoumi, A. Dafali, M. Bakasse, M. A. El Mhammedi and M. Abdennouri, *J. Mater. Res. Technol.*, 2019, **8**, 6336–6353.

28 A. El-Faham, S. Osman, H. Al-Lohedan and G. El-Mahdy, *Molecules*, 2016, **21**, 714.

29 Z. Lakbaibi, M. Damej, A. Molhi, M. Benmessaoud, S. Tighadouini, A. Jaafar, T. Benabbouha, A. Ansari, A. Driouich and M. Tabyaoui, *Heliyon*, 2022, **8**, e09087.

30 S. Kr. Saha, M. Murmu, N. C. Murmu and P. Banerjee, *J. Mol. Liq.*, 2022, **364**, 120033.

31 H. Ferkous, S. Djellali, R. Sahraoui, Y. Benguerba, H. Behloul and A. Çukurovali, *J. Mol. Liq.*, 2020, **307**, 112957.

32 A. Fellah, Y. Harek, I. Ichchou, L. Larabi, H. Rouabhi, R. Bourzami and A. Ammari, *Colloids Surf. Physicochem. Eng. Asp.*, 2024, **685**, 133150.

33 K. Cherrak, M. E. Belghiti, A. Berrissoul, M. El Massaoudi, M. El Faydy, M. Taleb, S. Radi, A. Zarrouk and A. Dafali, *Surf. Interfaces*, 2020, **20**, 100578.

34 P. P. Kumari, P. Shetty, S. A. Rao, D. Sunil and T. Vishwanath, *Bull. Mater. Sci.*, 2020, **43**, 46.

35 O. S. I. Fayomi, I. G. Akande, A. P. I. Popoola and H. Molifi, *J. Mater. Res. Technol.*, 2019, **8**, 3088–3096.

36 L. M. Shaker, A. A. Al-Amiery, M. A. I. Al-Hamid and W. K. Al-Azzawi, *Koroze Ochr. Mater.*, 2024, **68**, 9–21.

37 A. Chaouiki, M. Chafiq, A. H. Al-Moubaraki, M. Bakhouch, M. El Yazidi and Y. G. Ko, *Arab. J. Chem.*, 2022, **15**, 104323.

38 J. A. Gauthier, S. Ringe, C. F. Dickens, A. J. Garza, A. T. Bell, M. Head-Gordon, J. K. Nørskov and K. Chan, *ACS Catal.*, 2019, **9**, 920–931.

39 L. Ahmed, N. Bulut, O. Kaygili and R. Omer, *J. Phys. Chem. Funct. Mater.*, 2023, **6**, 34–42.

40 S. Malinowski, M. Wróbel and A. Woszuk, *Materials*, 2021, **14**, 6197.

41 O. E. Oyeneyin, N. D. Ojo, N. Ipinloju, E. B. Agbaffa and A. V. Emmanuel, *Beni-Suef Univ. J. Basic Appl. Sci.*, 2022, **11**, 132.

42 M. Murmu, S. Kr. Saha, P. Bhaumick, N. C. Murmu, H. Hirani and P. Banerjee, *J. Mol. Liq.*, 2020, **313**, 113508.

43 N. Z. K. Razali, W. N. S. Wan Hassan, S. A. I. Sheikh Mohd Ghazali, S. N. Mohd Shotor and N. N. Dzulkifli, *Chem. Pap.*, 2024, **78**, 715–731.

44 H. Lgaz, R. Salghi, S. Masroor, S.-H. Kim, C. Kwon, S. Y. Kim, Y.-J. Yang and I.-M. Chung, *J. Mol. Liq.*, 2020, **308**, 112998.

45 H. El Hassouni, A. Elyousfi, F. Benhiba, N. Setti, A. Romane, T. Benhadda, A. Zarrouk and A. Dafali, *Inorg. Chem. Commun.*, 2022, **143**, 109801.

46 F. Ennafaa, A. Chraka, K. Tassaoui, I. Mouamr, M. Damej, A. E. L. Mahmoudi, K. Bougrin, H. T. Rahal and M. Benmessaoud, *Mater. Chem. Phys.*, 2025, **334**, 130441.

47 A. Omari Alaoui, W. Elfalleh, B. Hammouti, A. Titi, M. Messali, S. Kaya, B. El IBrahimi and F. El-Hajjaji, *RSC Adv.*, 2025, **15**, 12645–12652.

48 A. Acidi, A. Sedik, A. Rizi, R. Bouasla, K. O. Rachedi, M. Berredjem, A. Delimi, A. Abdennouri, H. Ferkous, K. K. Yadav, M. Alam, B. Ernst and Y. Bengureba, *J. Mol. Liq.*, 2023, **391**, 123423.

49 R. Sghyar, Y. Rhazi, M. Aloui, M. Lahyaoui, H. Elmrayej, H. Elmsellem, O. Abdellaoui, N. Aflak, O. Moussaoui, M. M. Alanazi, A. Kabra, E. M. E. Hadrami, E. H. Mabrouk and N. K. Sebbar, *ACS Omega*, 2025, **10**, 2069–2080.

50 V. Choudhary, S. Dua, N. Arora, R. C. Saxena, B. G. Prakashaiah, T. Senthilkumar, M. M. Singh, T. S. Khan and S. K. Ganguly, *Discover Chem.*, 2025, **2**, 44.

51 K. A. Alamry, A. Khan, J. Aslam, M. A. Hussein and R. Aslam, *Sci. Rep.*, 2023, **13**, 6724.

52 L. Chahir, N. Benzbiria, F. Z. Tahri, M. El Faydy, F. Benhiba, D. Benmessaoud Left, M. Zertoubi, I. Warad, M. Allali, K. Bougrin and A. Zarrouk, *Phys. Chem. Chem. Phys.*, 2024, **26**, 23766–23783.

53 N. N. Hau and D. Q. Huong, *J. Mol. Struct.*, 2023, **1277**, 134884.

54 M. A. Hegazy, A. M. Badawi, S. S. Abd El Rehim and W. M. Kamel, *Corros. Sci.*, 2013, **69**, 110–122.

55 K. Tassaoui, M. Damej, A. Molhi, A. Berisha and M. Errili, *Int. J. Corros. Scale Inhib.*, 2022, **11**(1), 1–464.

56 N. Betti, A. A. Al-Amiery, W. K. Al-Azzawi and W. N. R. W. Isahak, *Sci. Rep.*, 2023, **13**, 8979.

57 N. Mouats, S. Djellali, H. Ferkous, A. Sedik, A. Delimi, A. Boublia, K. O. Rachedi, M. Berredjem, A. Çukurovali, M. Alam, B. Ernsti and Y. Benguerba, *ACS Omega*, 2024, **9**, 27945–27962.

58 D. M. Jamil, H. S. Aljibori and A. Alamiery, *Results Chem.*, 2025, **15**, 102193.

59 J. P. Sheehan and T. M. Phan, *Biochemistry*, 2001, **40**, 4980–4989.

60 Y. M. Abdallah, O. A. El-Gammal, H. M. Abd El-Lateef and K. Shalabi, *RSC Adv.*, 2022, **12**, 14665–14685.

61 L. Chen, D. Lu and Y. Zhang, *Materials*, 2022, **15**, 2023.

62 M. A. Bedair, *Results Surf. Interfaces*, 2025, **19**, 100511.

63 R. H. Fowler, *Math. Proc. Camb. Phil. Soc.*, 1935, **31**, 260–264.

64 A. Kokalj, *Corros. Sci.*, 2023, **217**, 111112.

65 H. N. Tran, *Adsorpt. Sci. Technol.*, 2022, **2022**, 5553212.

66 M. Oubaaqa, M. Ouakki, M. Rbaa, A. S. Abousalem, M. Maatallah, F. Benhiba, A. Jarid, M. Ebn Touhami and A. Zarrouk, *J. Mol. Liq.*, 2021, **334**, 116520.

67 R. Aslam, G. Serdaroglu, S. Zehra, D. Kumar Verma, J. Aslam, L. Guo, C. Verma, E. E. Ebenso and M. A. Quraishi, *J. Mol. Liq.*, 2022, **348**, 118373.

68 L. K. M. O. Goni, I. Y. Yaagoob, M. A. J. Mazumder and S. A. Ali, *RSC Adv.*, 2024, **14**, 9725–9746.

69 R. Jalab, A. Al-Harbi, N. U. S. Riyaz, M. Shkoor, M. Khaled, A. Dawoud, M. Saad, I. Hussein, M. W. Wong, L. Wang, N. Alateyah, H. Abou-Saleh, A. S. A. Hatab and O. C. S. Al-Hamouz, *Discov. Appl. Sci.*, 2024, **6**, 641.

70 E. Ech-chihbi, B. Es-Sounni, C. Kerdoune, A. Mouhib, M. Bakhouch, R. Salim, R. Salghi, B. Hammouti, N. Mazoir, M. Chafiq, A. Chaouiki and Y. G. Ko, *Colloids Surf. Physicochem. Eng. Asp.*, 2024, **702**, 135073.

71 K. Xhanari, M. Farruku, A. Berisha, B. Seiti, K. Xhaxhiu, E. Kokalari and A. Lame, *Results Chem.*, 2025, **13**, 101922.

72 A.-R. El-Sayed, M. M. El-Hendawy, M. S. El-Mahdy, F. S. M. Hassan and A. E. Mohamed, *Sci. Rep.*, 2023, **13**, 4812.

73 X. Zhang, Y. Zhang, Y. Su, X. Wang and R. Lv, *ACS Omega*, 2022, **7**, 32208–32224.

74 M. Akbari Shahmirzadi and M. Azadi, *Heliyon*, 2024, **10**, e29962.

75 A. G. Sayed, A. M. Ashmawy, W. E. Elgammal, S. M. Hassan and M. A. Deyab, *Sci. Rep.*, 2023, **13**, 13761.

76 *MarvinSketch (Version 23)*, ChemAxon, 2023.

77 L. Adlani, N. Benzbiria, A. Titi, N. Timoudan, I. Warad, A. AlObaid, B. M. Al-Maswari, F. Benhiba, R. Touzani, H. Zarrok, F. Bentiss, H. Oudda and A. Zarrouk, *ACS Omega*, 2024, **9**, 13746–13763.

78 P. Geerlings, F. De Proft and W. Langenaeker, *Chem. Rev.*, 2003, **103**, 1793–1874.

79 B. El Ibrahimi, *Colloid Interface Sci. Commun.*, 2020, **37**, 100279.

80 E. H. El Assiri, M. Driouch, J. Lazrak, Z. Bensouda, A. Elhaloui, M. Sfaira, T. Saffaj and M. Taleb, *Heliyon*, 2020, **6**, e05067.

81 J. Ebrahimian, M. Khayatkashani, N. Soltani, Q. A. Yousif and M. Salavati-Niasari, *Arab. J. Chem.*, 2022, **15**, 103758.

82 N. Q. Su and X. Xu, *J. Chem. Phys.*, 2021, **154**, 174101.

83 R. A. Miranda-Quintana, F. Heidar-Zadeh, S. Fias, A. E. A. Chapman, S. Liu, C. Morell, T. Gómez, C. Cárdenas and P. W. Ayers, *Front. Chem.*, 2022, **10**, 929464.

84 S. Hadisaputra, A. Purwoko, F. Wajdi, I. Sumarlan and S. Hamdiani, *Int. J. Corros. Scale Inhib.*, 2019, **8**(3), 673–688.

85 A. I. Aljameel, *Int. J. Electrochem. Sci.*, 2022, **17**, 220524.

86 D. S. Chauhan, M. A. J. Mazumder, M. A. Quraishi and K. R. Ansari, *Int. J. Biol. Macromol.*, 2020, **158**, 127–138.

87 H. Lgaz, A. Aldalbahi and H.-S. Lee, *Molecules*, 2024, **29**, 5123.

88 K. Kousar, M. Dowhyj, M. S. Walczak, T. Ljungdahl, A. Wetzel, H. Oskarsson, A. S. Walton, P. Restuccia, N. M. Harrison and R. Lindsay, *Faraday Discuss.*, 2022, **236**, 374–388.

89 Y. H. Azeez, D. M. Mamand, R. A. Omer, A. H. Awla and K. A. Omar, *Corros. Rev.*, 2024, **42**, 775–793.

90 X.-L. Li, B. Xie, C. Lai, J.-S. Feng, X.-Q. Liu, L. Chen, Y.-G. Yang, R.-W. Ji, J.-Y. He, W. Li and M.-N. Liu, *J. Mol. Liq.*, 2022, **355**, 118926.

91 M. Murmu, N. C. Murmu, M. Ghosh and P. Banerjee, *J. Adhes. Sci. Technol.*, 2022, **36**, 2732–2760.

92 G. Xiong, W. Zhenxing, Y. Jiacai, Y. Zhijiang, H. Changyu and Y. Mingzhu, *Nucleic Acids Res.*, 2021, **49**, W1–W14.

93 R. G. M. D. A. Macedo, N. D. N. Marques, J. Tonholo and R. D. C. Balaban, *Carbohydr. Polym.*, 2019, **205**, 371–376.

94 C. N. A. Azmi, S. S. Azahar, N. A. N. Shamsulazri, T. S. Hamidon, M. H. Hussin, T. W. Nee, S. Sabar and E. N. M. Yusof, *Int. J. Biol. Macromol.*, 2024, **282**, 137200.

95 M. P. Binsi, T. K. Joby, K. Ragi, V. C. Sini and J. Reeja, *Curr. Chem. Lett.*, 2020, 19–30.

96 A. S. Fouda, S. A. A. El-Maksoud, A. El-Hossiany and A. Ibrahim, *Int. J. Electrochem. Sci.*, 2019, **14**, 6045–6064.